8-27-2012

The effect of carbon dioxide on the density and compressibility of kimberlitic magma

Alison R. Santos

Alison R. Santos
Candidate

Earth and Planetary Sciences
Department

This thesis is approved, and it is acceptable in quality and form for publication:

Approved by the Thesis Committee:

Dr. Carl Agee, Chairperson

Dr. Francis McCubbin

Dr. Tobias Fischer

THE EFFECT OF CARBON DIOXIDE ON THE DENSITY AND COMPRESSIBILITY OF KIMBERLITIC MAGMA

by

ALISON R. SANTOS

BACHELOR OF SCIENCE, GEOLOGICAL SCIENCES,
SALEM STATE UNIVERSITY, 2010

THESIS

Submitted in Partial Fulfillment of the
Requirements for the Degree of

Master of Science
Earth and Planetary Sciences

The University of New Mexico
Albuquerque, New Mexico

July 2012

ACKNOWLEDGEMENTS

I would like to thank Mike Spilde for his assistance with the electron microprobe, Whitney McCutcheon for her assistance conducting the FTIR analyses, and Dr. Francis McCubbin for his help with experimental design and instruction in the laboratory. I would also like to thank Dr. Carl Agee for his role as advisor and for all of the help he provided during the course of this project, and my Thesis Committee, including Dr. Agee, Dr. McCubbin, and Dr. Tobias Fischer, for their assistance in this endeavor. Thank you to the other students in the High Pressure Laboratory for their support, for showing me the ropes, and for being there to make this learning process easier and more fun than it would have been alone.

THE EFFECT OF CARBON DIOXIDE ON THE DENSITY AND COMPRESSIBILITY OF KIMBERLITIC MAGMA

by

Alison R. Santos

B.S., Geological Sciences, Salem State University, 2010

M.S., Earth and Planetary Sciences, University of New Mexico, 2012

ABSTRACT

Constraints were placed on the density of kimberlitic melts containing varying amounts of CO_2 using high pressure sink/float experiments. The melt composition used was carefully selected and was prepared free of H_2O and minor elements in order to focus on the effect of CO_2. Experiments were run in graphite capsules over a pressure range of 4-10 GPa in a multi-anvil apparatus using Fo_{100} and Fo_{90} spheres as density markers. The compositions used contained 0, 3, 6, and 12 wt% CO_2 and were derived from mixing the 0 and 12 wt% CO_2 compositions together. Run products were analyzed with FTIR to confirm the presence of carbonate and lack of water and with EPMA to verify the composition. Carbon was quantified using the by difference method, but plans are in place to develop a method to quantify this element by EPMA. The density data places constraints on the location of the melt compression curves, and shows the melts to be eruptible from pressures below 9 GPa (10 GPa for the 6 wt% CO_2 composition) on Earth. This data is also applicable to Venus, and all compositions are eruptible from up to 9 GPa according to current Venus mantle density models.

TABLE OF CONTENTS

LIST OF FIGURES

LIST OF TABLES

Chapter 1

Background and Previous Studies

Introduction

Carbon is present throughout the solar system in planetary atmospheres (Mars, Earth, Venus), molten material (Earth), and in solid rocky bodies (Earth, Mars, meteorites). Carbon is found in a variety of oxidation states in these different locations, from metal carbides to carbonate (CO_3^{2-}) (e.g. Hirschmann and Withers 2008). At this time, the most detailed picture of the presence and many roles of carbon is found on Earth. Carbon on Earth is cycled through all of Earth's systems through various biological, atmospheric, and geological processes. Carbon is heavily involved in biological processes, being a major constituent of organic molecules and a by-product of animal respiration (as CO_2). It is also present in the atmosphere in many forms (CO_2, CH_4, CO, etc.), and has recently been in focus due to concerns about greenhouse gases. The geosphere also contains carbon in the form of carbonate minerals and associated rocks, the mineral graphite, and as the carbonate anion incorporated into a variety of other mineral structures.

While carbon on Earth is greatly important for life, it also plays a large role in geologic processes. Reduced forms of carbon such as diamonds often contain fluid inclusions, which provide a record of mantle conditions that are otherwise inaccessible for observation (Klein-BenDavid et al. 2004). More oxidized forms of carbon, such as CO_2, play important roles in magmatism. CO_2 has been found in nearly every magma type on Earth, solidifying its place as the second most abundant magmatic volatile (water being the first). Some exotic magma types, including carbonated silicate magmas such as kimberlites and lamproites, and carbonate magmas such as carbonatites, contain large

amounts of CO_2 (greater than 5 weight per cent) and have been studied for clues to their origin (Mitchell 1997). For the duration of this work, the term "carbonated silicate magmas" will be used for any silicate magma containing any quantity of dissolved CO_2, while the term "carbonate magma" will refer to magmas that have carbonate as their main component. The term "carbonated magmas" refers to any type of magma containing dissolved CO_2. When CO_2 is dissolved in silicate magmas (in the form of the carbonate anion in the case of mafic magmas (Eggler and Rosenhauer 1978), which are considered here), it changes the physical properties of the magma, particularly those properties related to eruptibility, such as density, viscosity, and wetting ability (Spera 1984, Guillot and Sator 2011). Determining how dissolved CO_2 changes these properties over a range of pressures and temperatures has been a topic of study for many years, and many advances in understanding the effects of CO_2 on magma properties have been made. The effect of dissolved CO_2 on magma density has been studied in particular, with numerous workers investigating different pressure ranges and magma compositions. A brief summary of their work follows.

Previous Studies

Carbonated basalt, peridotite, komatiite, and kimberlite have been investigated over a range of pressures and CO_2 contents. Equations of State (EOS) describing the behavior of melt density with changes in pressure and temperature are often used in these studies because the studies cover a range of pressures, and it makes such data easier to compare between studies or be applied by other workers. Typically, the third order Birch-Murnaghan Equation of State (BM3) is applied to describe silicate melt behavior (Birch 1952). This EOS uses the parameters of K_T (bulk modulus, the inverse of compressibility), K' (pressure derivative of the bulk modulus), zero pressure density, and

density at the pressure of interest. Higher K_T values indicate lower compressibility, and higher K' values indicate greater changes to the bulk modulus with changes in pressure. Table 1 shows the EOS parameters for the different melt compositions and CO_2 contents determined from previous studies that utilize different techniques (described in Appendix D). When CO_2 is added to each melt composition, the melt becomes more compressible. The K' for each composition only varies slightly between the CO_2-free and carbonated versions of each composition, typically staying the same or increasing only slightly.

Table 1: EOS parameters determined for carbonated melts from previous studies.

Composition (wt% CO_2)	Derivation Temperature (K)	K_T (GPa)	K'	Method	Source
MORB (0)	2200	18.7	5	Sink/Float	Ohtani and Maeda 2001
MORB (5)	2300	17	5	Sink/Float	Ghosh et al. 2007
MORB (0)	2273	13.3	8.31	Molecular Dynamics	Guillot and Sator 2011
MORB (2)	2273	11.2	9.66	Molecular Dynamics	Guillot and Sator 2011
MORB (5)	2273	10.6	9.43	Molecular Dynamics	Guillot and Sator 2011
Kimberlite (0)	2273	37.21	4.35	Molecular Dynamics	Guillot and Sator 2011
Kimberlite (2)	2273	29.35	5.85	Molecular Dynamics	Guillot and Sator 2011
Kimberlite (5)	2273	24.19	6.53	Molecular Dynamics	Guillot and Sator 2011
Kimberlite (10)	2273	18.55	7.3	Molecular Dynamics	Guillot and Sator 2011
Peridotite (0)	2100	24	7.3	X-ray Absorption	Sakamaki et al. 2010
Peridotite (2.5)	1800	23	8.5	X-ray Absorption	Sakamaki et al. 2011
Komatiite (0)	1850	22.89	3.1	Sink/Float	Duncan and Agee 2011
Komatiite (5)	1850	17.22	3.1	Sink/Float	Duncan and Agee 2011

In all of the studies shown in Table 1, the addition of CO_2 to a silicate melt decreases the melt density over a wide pressure range (shown in Figure 1). This density decrease typically leads to carbonated melts being buoyant at greater depths than non-carbonated melts, despite their greater compressibility. There exists the possibility that carbonated melts will become more dense than their non-carbonated equivalents at high pressure due to the higher compressibility of carbonated melts, but this behavior does not

seem to occur at pressures less than 10 GPa in any previous melt density studies, as shown in Figure 1.

All of the previous studies mentioned so far only apply their data to terrestrial magmatism, but it is relevant to any rocky body that can produce carbonated melts. For example, Venus shows evidence of producing carbonated silicate melts and carbonate melts (further discussed in Chapter 4). While application of melt density data is not as easy or certain on other planetary bodies due to a lack of seismic data and thus a lack of a mantle density profile, it is still possible. Different planetary bodies will have different mantle density profiles, and as a result, the effect of volatiles on melt eruptibility could be vital to having deep source magmatism.

In an effort to better understand kimberlite volcanism, deep earth magmatism, and magmatism on Venus, this study focuses on the effect of dissolved CO_2 on silicate melt density. We use high pressure experiments on a kimberlitic melt composition with varying amounts of CO_2 to attempt to systematically examine what effect different amounts of CO_2 have on melt density. A better understanding of how CO_2 affects melt properties will help our understanding of kimberlites, deep Earth magmatic processes, and can begin to enhance our understanding of magmatism on Venus.

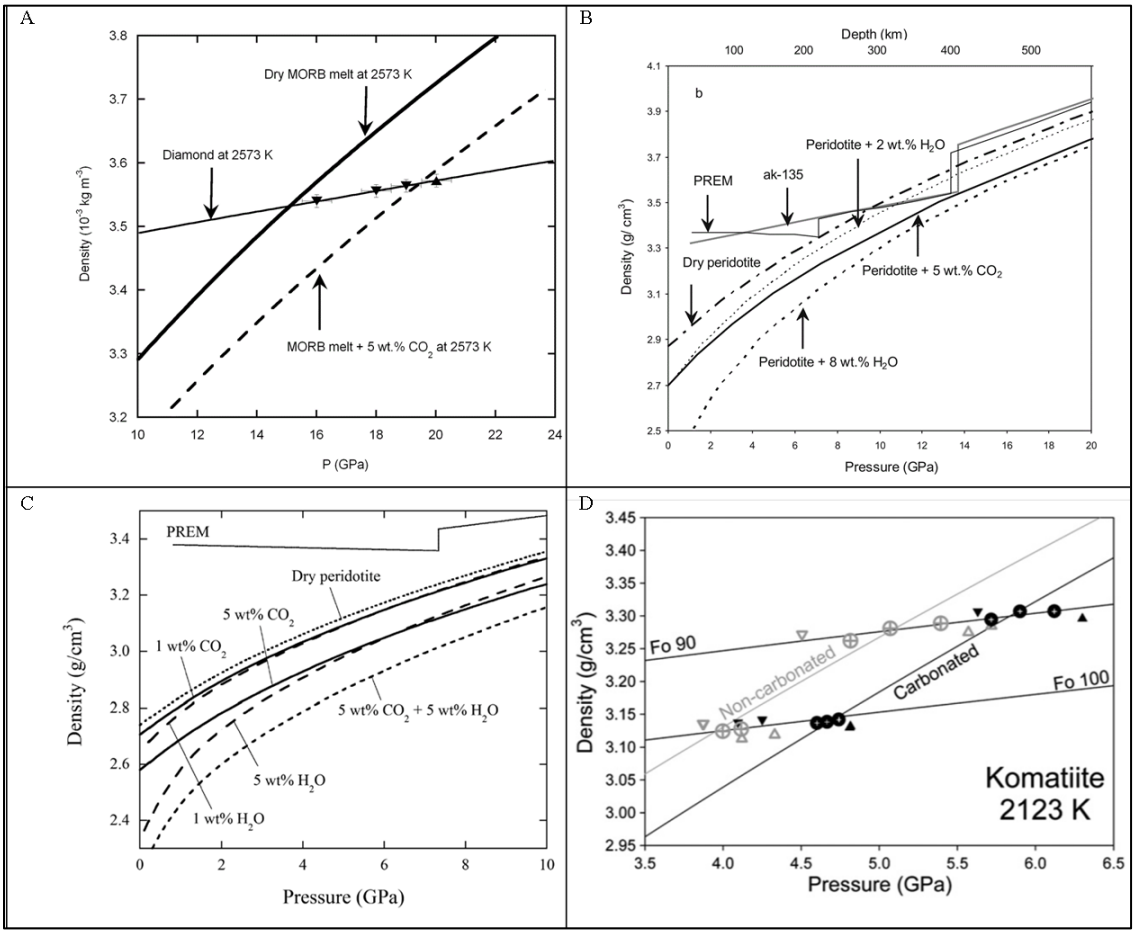

Figure 1: Results of previous carbonated melt density studies. A: Mid-ocean ridge basalt (MORB) compression curves derived by Ghosh et al. (2007). The compression curve of diamond is also shown for reference. B: Peridotite compression curves derived by Ghosh et al. (2007). The K_T and K' values were calculated based on their experimental results using a MORB composition. The Preliminary Reference Earth Model (PREM) (Dziewonski and Anderson 1981) is shown to illustrate density crossovers between these melts and the mantle. C: Peridotite melt compression curves showing peridotite with varying amounts of CO_2 and H_2O versus PREM (Sakamaki et al. 2011). Density data for these melts were obtained using the X-ray absorption method. D: Komatiite compression curves from Duncan and Agee (2011) plotted with compression curves for forsterite olivines (90% forsterite, Fo_{90}, and 100% forsterite, Fo_{100}). (continued on next page)

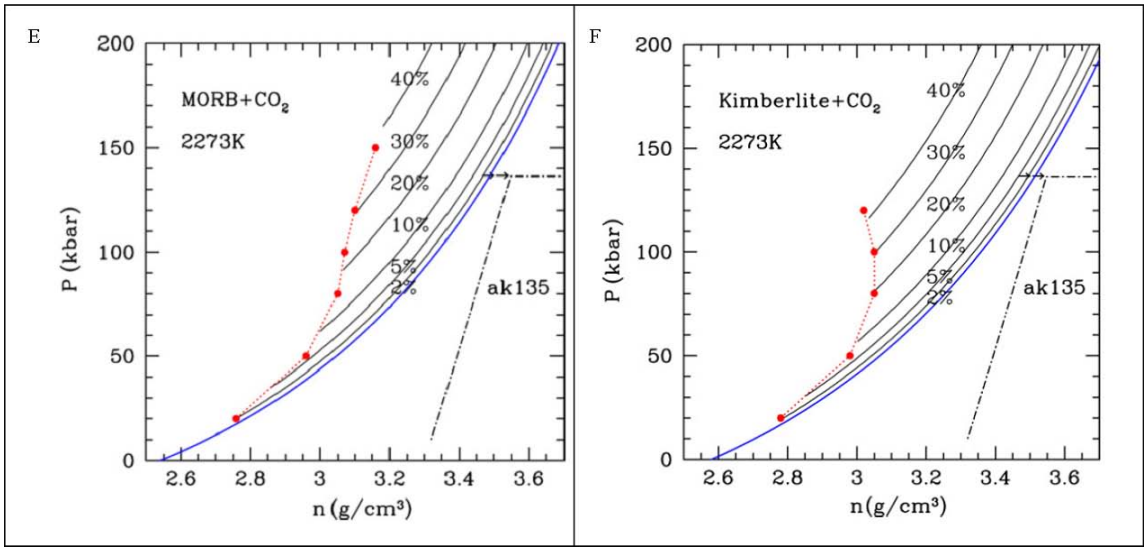

Figure 1 (con't.): E: MORB compression curves showing density behavior for varying amounts of CO_2. Curves were derived using molecular dynamics simulations (Guillot and Sator 2011). F: Kimberlite compression curves for varying amounts of CO_2 determined using molecular dynamics simulations (Guillot and Sator 2011).

Chapter 2

Experimental Procedures

Introduction

In this study, we wanted to focus on the effect on density of relatively large amounts of CO_2 dissolved in silicate melts. A prime candidate composition for this goal is a kimberlite magma, as kimberlites are natural magmas that contain high amounts of volatiles. Natural kimberlites also have their own set of questions, such as their ascent mechanism, petrogenesis, and relationship to plate tectonics, and a density study on these magmas can help in the search for answers to these questions. Kimberlites are discussed in more detail in Chapter 3, but an example of how melt density can aid in understanding kimberlites is with regard to their source region. Previous studies have tried to determine the source material and source depth for kimberlites by way of melting experiments using mantle materials (e.g. Gudfinnsson and Presnall 2005, Canil and Scarfe 1990) or crystallization experiments using kimberlite materials (e.g. Mitchell 2004). While these studies provided valuable results (discussed further in Chapter 3), looking at these questions using melt density data is a different approach that can provide further insight into the depth of kimberlite formation. Melt density data can constrain the depth of formation of melts by determining density crossover points between the mantle and the melt. Density crossover points are points in density-pressure space where the density of the melt changes from being either less dense than the surrounding mantle to being more dense than the surrounding mantle, or from being more dense than the surrounding mantle to being less dense than the surrounding mantle (shown in Figure 2). A density crossover that results in the melt becoming more dense than the mantle shows the highest pressure the melt can originate from, as the melt must be less dense than its surroundings

to be able to erupt. With this study, we aim to provide experimental constraints on the effect of dissolved CO_2 on melt density and examine what this means for kimberlitic melts on both Earth (Chapter 3) and Venus (Chapter 4).

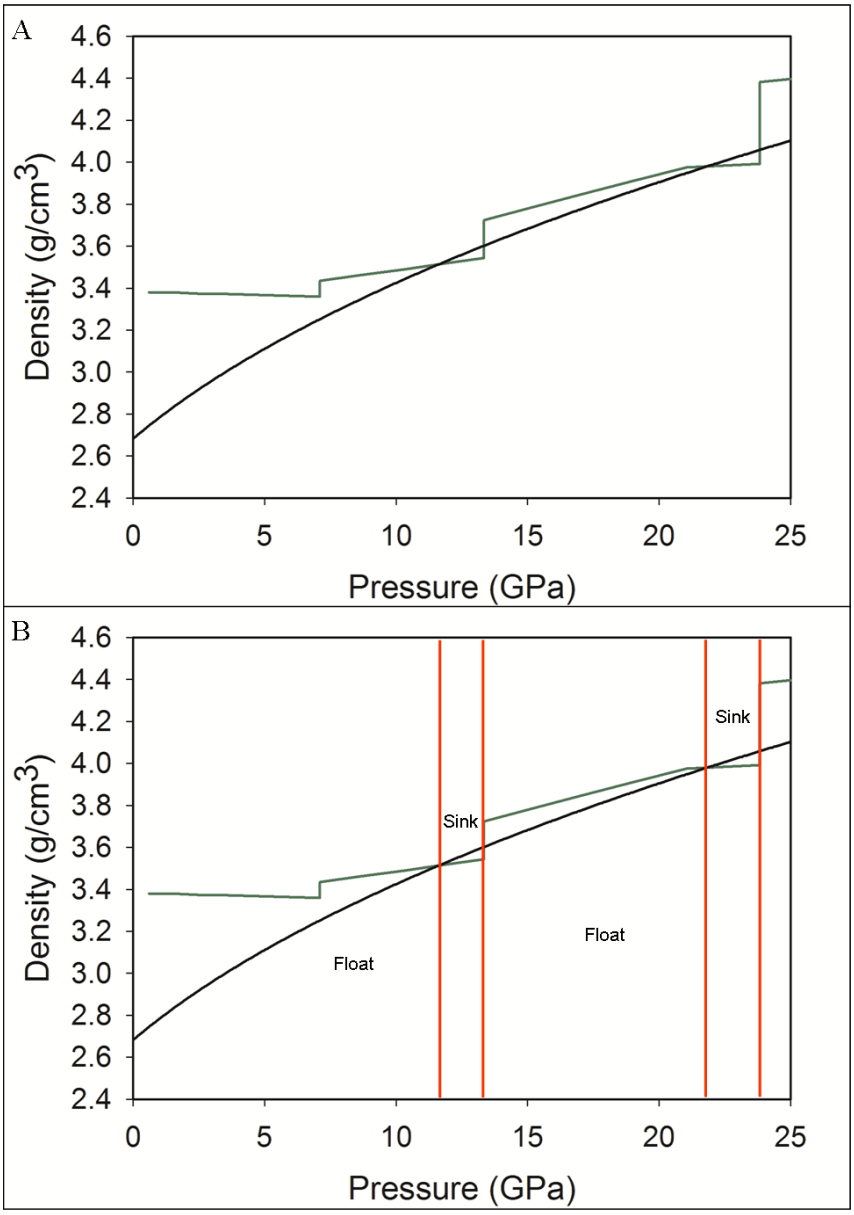

Figure 2: An example of density crossovers between a melt and the mantle. A: Graph of density vs. pressure showing a density profile for Earth's mantle in green (PREM from Dziewonski and Anderson 1981) and an example of melt compression curve derived using the BM3 equation in black. B: The same graph from A with density crossovers shown by red vertical lines. When the melt compression curve lies below PREM, the melt is less dense than the surrounding mantle and will float, when the melt compression curve is above PREM, the melt is more dense than the surrounding mantle and will sink. This melt would only be able to erupt if generated at pressures below 12 GPa (around 350 km depth) because a density crossover occurs at that pressure. If the melt is generated at pressures above 12 GPa, it will encounter the negative buoyancy zone between 12 and 13 GPa and will sink.

Composition Selection

As stated previously, the composition chosen for this study is based on a kimberlite magma, and in order to keep the results of this study as relevant to natural kimberlites as possible, we carefully considered what composition to select. No certain kimberlite parent magma composition exists, but many have been proposed (e.g. Kopylova et al. 2007, le Roex et al. 2006). Many difficulties exist in finding a parent magma, mainly stemming from extensive alteration and lack of preservation or discovery of quenched kimberlite glasses (Keshav et al. 2005). During ascent, kimberlites entrain mantle xenoliths, and the orthopyroxene from these xenoliths dissolves into the melt, resulting in an increase in melt SiO_2 and decrease in melt volatiles (Kopylova et al. 2007). Kimberlites range in age from late Precambrian to Cretaceous, so they have been largely exposed to surface and crustal alteration environments for long periods of time (Keshav et al. 2005). Kimberlites are particularly affected by serpentinization once erupted, which causes removal of Ca and CO_2 from the kimberlite and addition of Si, Mg, and H_2O, causing compositional and mineralogical changes (Sparks et al. 2009).

The proposed parental kimberlite magma used for this study is based on that of Kopylova et al. (2007). We selected this composition because we felt it was a good representation of a kimberlite melt with minimal alteration. Kopylova et al. (2007) determined this composition by analyzing natural kimberlite samples and then calculating out 6 volume per cent orthopyroxene from these analyses; this amount of orthopyroxene was determined based on the amount of olivine present in mantle xenoliths and the amount of mantle xenoliths present in the analyzed kimberlite. While this composition was corrected for some of the alteration expected in kimberlite magmas, it still is in

compositional agreement with other natural kimberlite samples. The Kopylova et al. (2007) composition, along with 356 others from various sources, was plotted in a ternary plot of SiO_2-CaO-MgO (Figure 3), and the chosen composition falls within the cluster of other available kimberlite data (Kjarsgaard et al. 2009, Sparks et al. 2009, Harris et al. 2004, Patterson et al. 2009). The composition is listed in Table 2. Because the primary focus of this study is on CO_2, the composition of Kopylova et al. (2007) was simplified by removing H_2O and minor elements, and the simplified compositions are also listed in Table 2.

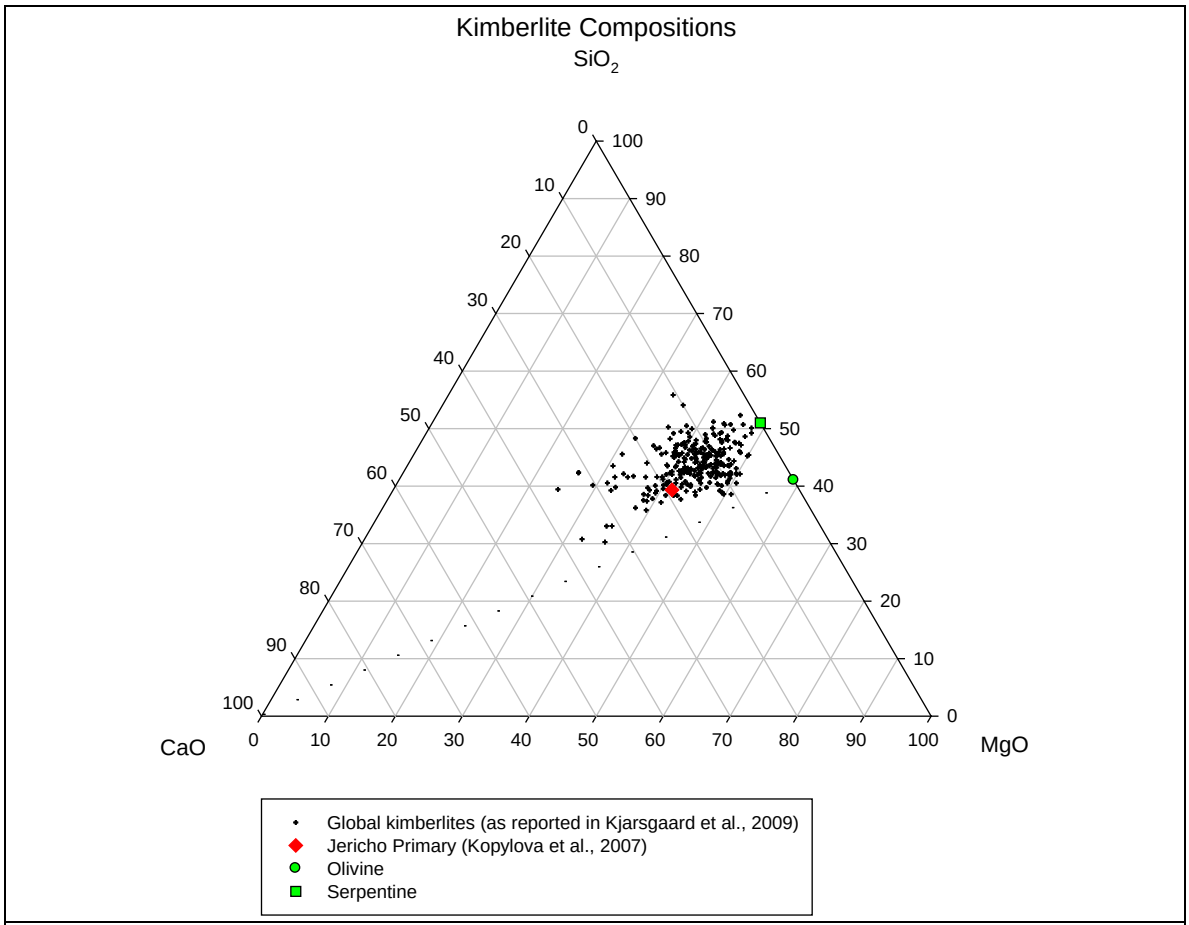

Figure 3: Ternary plot from Sparks et al. (2009) for examining kimberlite alteration. Kimberlite data is from listed sources. Sparks et al. (2009) propose unaltered kimberlites should fall on the line between olivine and the CaO apex. None of the kimberlites fall on this line, but the Jericho composition is relatively close to it without being an outlier to the majority of the other kimberlites.

Table 2: Kimberlite compositions relevant to this study. [1]-Kimberlite melt proposed by Kopylova et al. (2007) for the Jericho kimberlite, other compositions are based on the Jericho composition with minor elements and H_2O removed, and varying amounts of CO_2.

Oxide	Primitive Kimberlite Melt[1]	C100	C75	C50	C25	C0
SiO_2	26.70	29.44	30.43	31.41	32.40	33.38
TiO_2	1.73	1.91	1.97	2.04	2.10	2.16
Al_2O_3	1.57	1.73	1.79	1.85	1.90	1.96
Cr_2O_3	0.36	0.00	0.00	0.00	0.00	0.00
FeO_{total}	7.58	8.36	8.64	8.92	9.20	9.48
MnO	0.18	0.00	0.00	0.00	0.00	0.00
MgO	28.25	31.15	32.19	33.24	34.28	35.32
CaO	12.90	14.22	14.70	15.18	15.65	16.13
Na_2O	0.10	0.00	0.00	0.00	0.00	0.00
K_2O	1.26	1.39	1.44	1.49	1.53	1.58
P_2O_5	0.40	0.00	0.00	0.00	0.00	0.00
CO_2	9.88	11.81	8.86	5.91	2.95	0.00
H_2O	9.07	0.00	0.00	0.00	0.00	0.00
Total	99.98	100.01	100.02	100.04	100.01	100.01
Mg#	86.9	86.9	86.9	86.9	86.9	86.9

Experimental Methods

Experimental starting material was created by mixing reagent grade oxide and mineral powders. Iron was added in the form of Fe^{2+} using synthetic fayalite powder created by combining quartz (SiO_2) and hematite (Fe_2O_3) powders in a gas mixing furnace. CO_2 was added to the starting material using potassium and calcium carbonate powders (K_2CO_3 and $CaCO_3$ respectively). Oxide powders were combined using a mechanical agate mortar and pestle and were ground under ethanol. Two end member compositions were created, C0 and C100, containing 0 and 11.81 wt% CO_2 respectively. These compositions were then mixed together in ratios of 75:25, 50:50, and 25:75 to create compositions with 3 wt% (C25), 6 wt% (C50), and 9 wt% (C75) CO_2. Table 2

contains a list of all created compositions. After mixing, each composition was dried in a 110°C oven overnight to remove any adhered water and then stored in a desiccator. Composition C75 was not used for experimentation.

Experiments were run in a Walker-style multi-anvil using 6 and 8 mm TEL (truncated edge length) cell assemblies with WC cubes. Temperature was maintained during the experiment using W-Re thermocouple wires (W26% and W5%). Experimental run temperatures were chosen to be above the melt liquidus and below the liquidus of the density marker spheres. Temperature ramp rates were around 300°/minute. To determine the melt density at the experimental conditions, we used the sink/float method of Agee and Walker (1988). This method relies on finding the position of two mineral spheres in the experimental run product to determine density brackets which will constrain the melt density. Mineral spheres were between 300 and 700 microns in size for 8 mm TEL experiments and around 250 microns in size for 6 mm TEL experiments. The size of the spheres is limited by the size of the capsule. Spheres were created from gem quality crystals of synthetic pure forsterite (Fo_{100}) and San Carlos olivine (90% forsterite or Fo_{90}). Small pieces were broken off the crystals and placed in a Bond Air Mill and tumbled to create spheres of the desired size (Bond 1951). Experiments were run in graphite capsules, which have proven to retain CO_2 in the melt during a run. Graphite capsules also serve to keep the oxygen fugacity of the experiments near the GCO (graphite-CO) buffer.

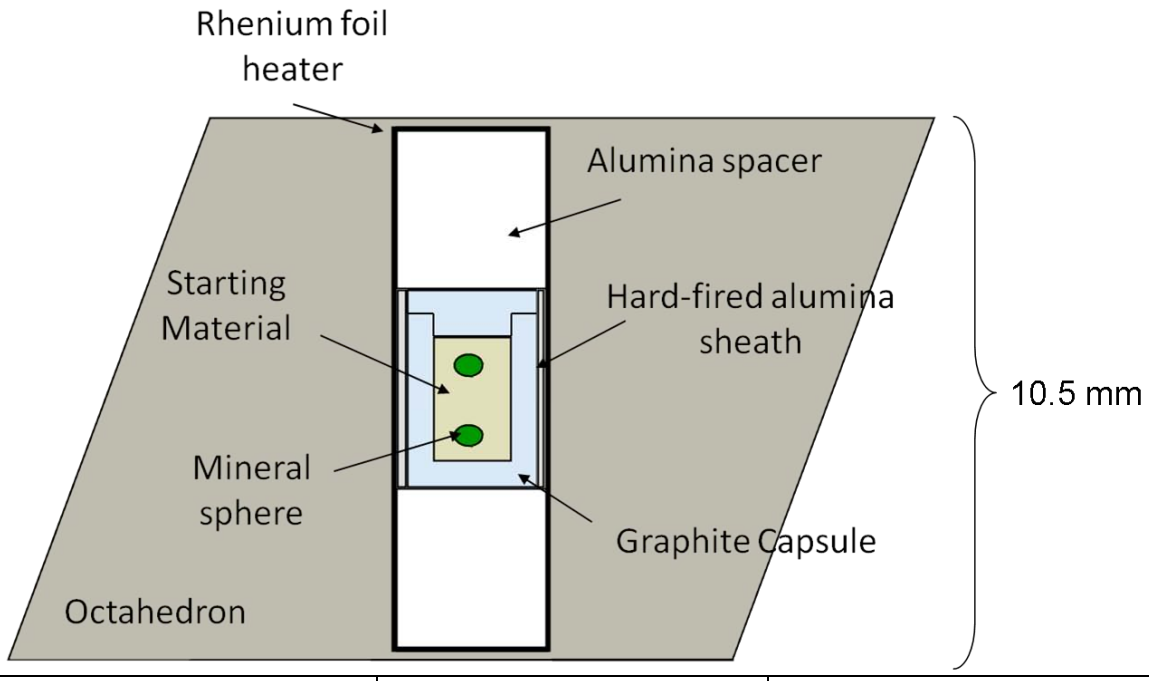

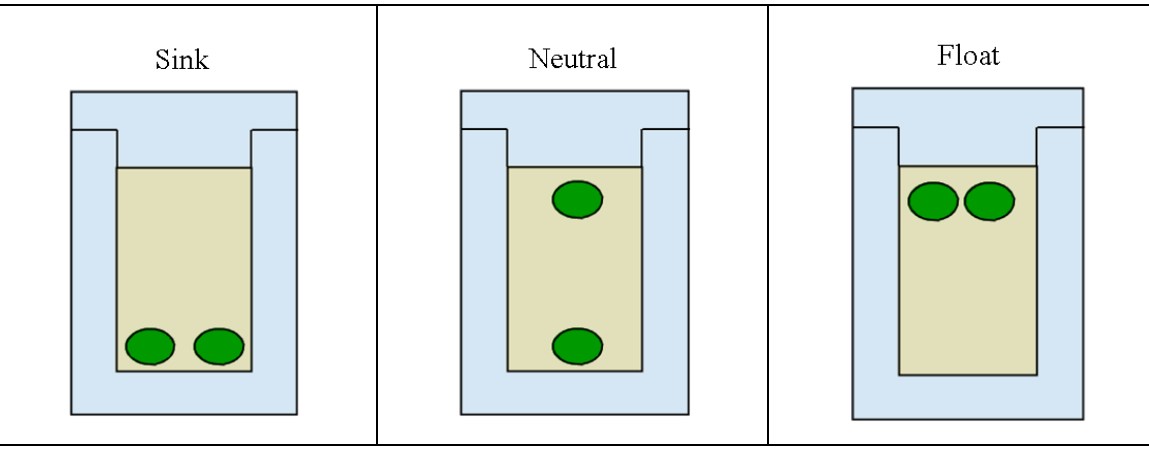

Figure 4: Experimental setup (top of figure) and different possible results (bottom).

Figure 4 illustrates the experimental setup for a sink/float run. The graphite capsule is loaded with alternating layers of sample and a mineral sphere with sample material at the bottom and top of the capsule. The starting material at the bottom and top serve to keep the spheres from touching the capsule, which could cause the spheres to stick and not move during the run. The filled capsule is loaded into a ceramic octahedron. The spacer material is crushable alumina, the sheath is hard-fired alumina, and the heater is made of rhenium foil. Run durations were around 30 seconds.

Run products were mounted in epoxy and ground using water and either SiC paper or diamond grinding discs. Sphere positions were recorded as spheres could not always be preserved if they were not found in the same plane in the capsule. Water and alumina powders were used to polish samples to a 0.3 micron finish in steps of 5, 1, and 0.3 microns. Many samples experienced extreme plucking during grinding (Figure 5), with large portions of the sample being removed. Run products that experienced plucking or ones that seemed in danger of experiencing it were plugged with epoxy. Areas of epoxy were avoided for all forms of sample analysis.

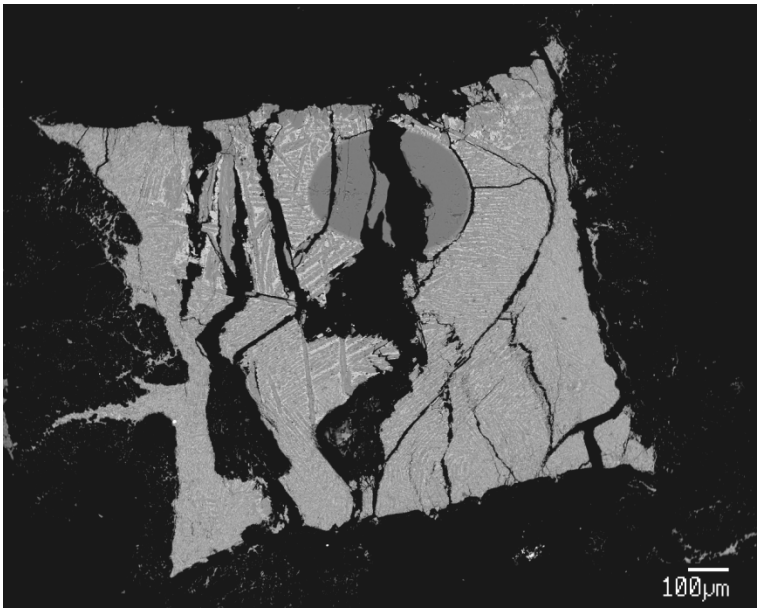

Figure 5: Backscattered electron (BSE) image of sample C50-005. Black regions within the sample area are where the sample has been plucked out during grinding.

Analyses

All experimental run products were analyzed using a JEOL 8200 electron microprobe. Samples were sonicated for approximately 30 seconds each in green soap, de-ionized water, acetone, and isopropyl alcohol to remove any leftover polishing material. Cleaned samples were then given an approximately 15-20 nm thick carbon

coat. All samples were analyzed with a 15 keV accelerating voltage, a beam current of $2x10^{-8}$ A, and a 20 μm beam diameter. Mineral spheres were analyzed with the same conditions and a 1 μm beam diameter. Carbon was not directly analyzed in the samples, but melt analyses showed low probe totals that correlated with the amount of carbon (as the component CO_2) present in the starting material (Table 3). This "by difference" method assumes the deficit in the microprobe totals is equal to the amount of CO_2 present in the run product (Dalton and Presnall 1998, Ghosh et al. 2007, Duncan and Agee 2011). In using the "by difference" method, the probe results indicate an increased carbon content in the run products; the "extra carbon" is likely only from the quench texture in the run product causing a low total and is not actually carbon.

Table 3: Carbon content of run products using the by difference method. The CO_2 content of each individual experiment is listed and the average CO_2 content is determined for each different starting material. The C50 composition shows the closest average CO_2 content to its ideal (CO_2 content of the starting material) value. The large range in CO_2 between experiments is likely due to low totals stemming from a heterogeneous sample surface and demonstrates the need to quantify carbon by a more reliable technique.

Carbon Contents Using By Difference Method (wt% CO_2)							
C100-006	12.62	**C50-002**	4.81	**C25-002**	1.82	**C0-006**	4.97
C100-007	14.69	**C50-003**	4.84	**C25-003**	4.49	**C0-010**	0.80
C100-010	17.49	**C50-005**	7.80	**C25-006**	6.35		
		C50-007	6.05	**C25-004**	4.08		
		C50-009	6.02				
Average	14.93	**Average**	5.82	**Average**	4.22	**Average**	2.89
Standard Deviation	2.44	**Standard Deviation**	1.72	**Standard Deviation**	2.28	**Standard Deviation**	2.95
Ideal CO_2 Content	11.81	**Ideal CO_2 Content**	5.91	**Ideal CO_2 Content**	2.95	**Ideal CO_2 Content**	0

Select run products from different compositions were chosen for micro-reflectance FTIR analyses. This data was collected using a Thermo-Nicolet Continuum Microscope attached to a Nexus 670 IR spectrometer. The instrument utilized a Globar

source, a KBr beam splitter, a collection range of 4000-400 cm^{-1}, a resolution of 4 cm^{-1}, and 128 scans for samples expected to have CO_3^{2-} and 512 scans for samples expected not to contain CO_3^{2-}. Aperture size was 100x100 μm. The FTIR analyses were used to confirm the presence of CO_3^{2-} in the run products. The samples chosen for analysis were from different pressures to assess whether or not CO_3^{2-} was retained over the range of experimental conditions.

Calculations

The densities of mineral spheres at experimental run conditions were calculated using the third order Birch-Murnaghan equation of state

$$P = \frac{3}{2}K_T\left[\left(\frac{\rho}{\rho_o}\right)^{7/3} - \left(\frac{\rho}{\rho_o}\right)^{5/3}\right]\left\{1 - \frac{3}{4}(4 - K')\left[\left(\frac{\rho}{\rho_o}\right)^{2/3} - 1\right]\right\}$$

where P is pressure (GPa), K_T is the isothermal bulk modulus, K' is its pressure derivative, ρ is the density at experimental P and temperature (T), and ρ_0 is the zero pressure density at experimental T. The zero pressure density is

$$\rho_{T,0} = \rho_{298}(T)exp\int_{298}^{T}\alpha(T)dT$$

where T is the experiment temperature, ρ_{298} is the density at standard temperature, and α is the thermal expansion ($\alpha(T) = a_0 + a_1T + a_2T^{-2}$). The parameters for each mineral are listed in Table 4. The mineral densities are used to represent the melt density at the pressure and temperature of the experiment, but are adjusted based on the analyzed melt composition and 1 bar melt densities (Appendix C).

Table 4: Thermoelastic parameters for olivine end members. For non-end member olivine it is assumed the parameters mix linearly. [a] Jacobs and De Jong (2007), [b] Liu and Li (2006), [c] Suzuki(1975), [d] Graham et al. (1988), [e] Isaak et al. (1993), [f] Suzuki et al. (1981), [g] Smyth (1975), [h] Hazen (1977).

Mineral	K_{298} (GPa)	K'	dK/dT	a_0 ($x10^{-5}$)	a_1 ($x10^{-9}$)	a_2
Forsterite	127.5[a]	4.8[a]	-0.02[b]	3.03	7.42	-0.5381[c]
Fayalite	134.6[d]	5.2[e]	-0.024[d]	0.239	11.53	-0.0518[f,g,h]

One bar melt densities were determined using data from Lange and Carmichael (1987) and Liu and Lange (2003). Large uncertainty is present in the 1 bar density information for CO_2 which creates large uncertainty in the 1 bar density values for the CO_2 bearing melts (Liu and Lange 2003). The 1 bar melt density serves as an anchor point for the melt's compression curve. Because melt composition changes slightly during an experiment due to reactions between the starting material and surrounding parts of the experimental assembly (e.g. mineral spheres, alumina sheath and spacers), the density data (mineral densities) were corrected for the changes in melt composition using the difference in 1 bar density of the ideal melt composition and the actual measured melt composition (correction to ideal composition). In order to create a compression curve for each melt, the corrected density points for each melt were then adjusted to be at the same temperature using a similar method as for the composition correction. The 1 bar melt density was calculated at the desired temperature and the difference between that density and the 1 bar density at the temperature of the experiment was added to the composition-corrected density. The corrected densities were then plotted, and the BM3 equation was fitted to the results.

Results

Experimental run conditions and results are listed in Table 5. Before the experimental results can be assessed, it is important to determine what the CO_2 contents

of the run products are. We were unable to directly analyze for carbon using the electron microprobe, but plan to do so in the near future to verify the results discussed here. Micro-reflectance FTIR analyses confirmed the presence of dissolved CO_2 in the form of carbonate in the compositions that were intended to have it, and also showed water was not present in the samples, results that show the melt densities observed were not influenced by other volatiles besides CO_2. A plot of reflectance data is shown in Figure 6. Peaks associated with water are not present, and the carbonate (CO_3^{2-}) peak is present around 1420 cm^{-1}. While there is no appropriate calibration to use reflectance FTIR to quantify the amount of carbonate in the samples, the different starting materials do show different carbonate peak intensities (Figure 6), which are roughly proportional to the amounts of CO_2 in the starting materials. The height of the silica peak around 900 cm^{-1} is variable between samples due to different amounts of mineralization due to quench crystals or equilibrium crystals in the run products. The presence of these crystals not only creates a heterogeneous sample surface, but it can affect the size, location, and shape of the carbonate peak, which prevents direct correlation of carbonate peak height to melt carbonate content. This effect is likely the reason the carbonate peak does not have its typical doublet shape, and also is a possible explanation for the similar carbonate peak height between the C100 (12 wt% CO_2) and C50 (6 wt% CO_2) compositions.

Table 5: Run conditions for sink/float experiments used in this study. All run durations were around 30 seconds.

	T (K)	P (GPa)	Sphere	Sphere Density (g/cm^3)	Melt Density (g/cm^3)	ρ_{2123} (g/cm^3)	Result
C100-006	2073	4	Fo_{100}	3.133	3.150	3.135	Sink
C100-007	2103	5	Fo_{100}	3.157	3.204	3.198	Sink
C100-010	2123	9	Fo_{100}	3.259	3.360	3.360	Sink
C50-002	2223	6	Fo_{100}	3.170	3.130	3.160	Neutral
C50-003	2223	5	Fo_{100}	3.143	3.107	3.137	Sink
C50-005	2323	7	Fo_{100}	3.186	3.228	3.287	Float
C50-007	2323	8	Fo_{90}	3.351	3.351	3.410	Sink
C50-009	2273	10	Fo_{90}	3.408	3.419	3.463	Float^
C0-006	2323	4	Fo_{100}	3.102	3.228	3.289	Sink
C0-010	2373	6	Fo_{100}	3.154	3.180	3.256	Sink*
C25-002	2323	5	Fo_{100}	3.131	3.091	3.151	Sink
C25-003	2373	6	Fo_{100}	3.154	3.186	3.261	Sink
C25-004	2448	8	Fo_{100}	3.200	3.230	3.326	Sink
C25-006	2398	9	Fo_{100}	3.232	3.319	3.401	Sink*

^-Results indicated a float, but must be verified due to heater failure during the run

*-Only one sphere was found in the run product on the bottom of the capsule

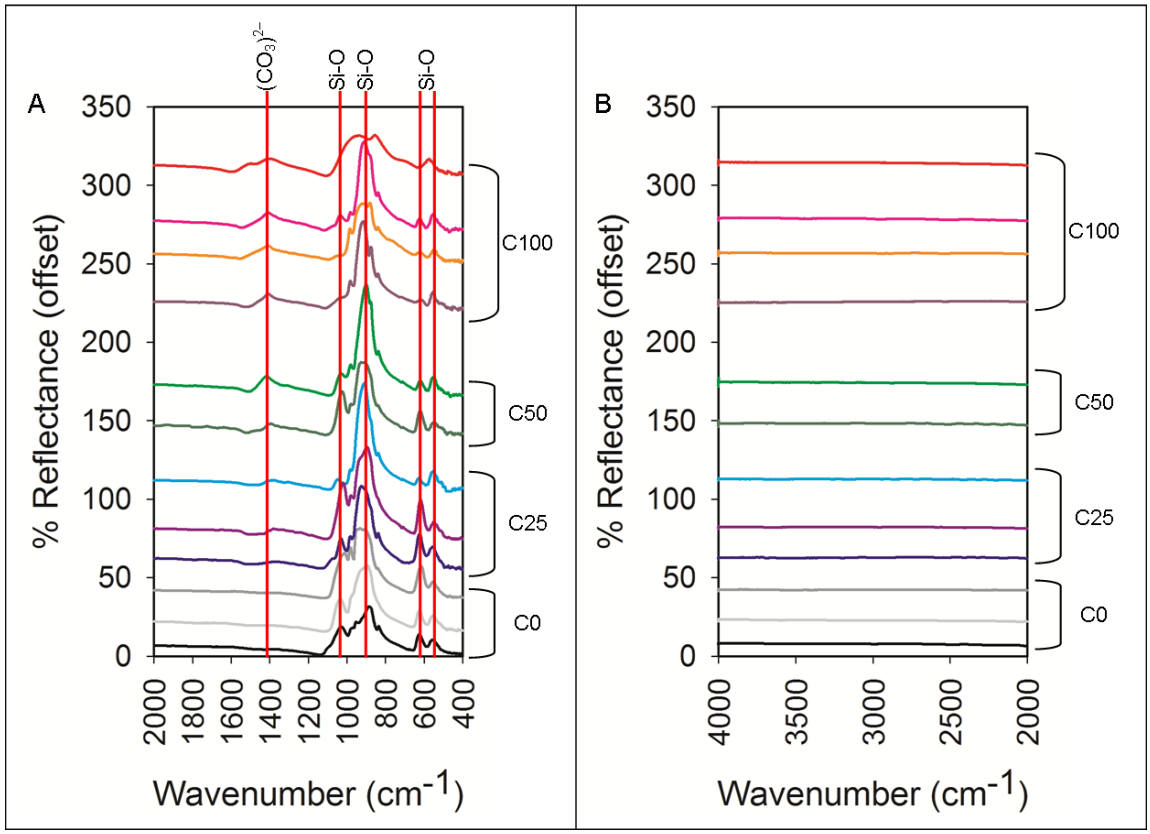

Figure 6: Micro-reflectance FTIR data. Run products from different starting materials are labeled. Note the % Reflectance values are offset. A: The carbonate peak is present around 1420 cm^{-1} and peaks associated with the various silicon-oxygen bonding environments are labeled Si-O. B: Micro-reflectance FTIR data over wavenumbers 4000-2000. The flat spectra show no indication of the presence of dissolved water (OH^-) in the run products.

As mentioned previously, there is no FTIR quantification method for carbon in these run products, and the best method for quantification at this time is the "by difference" method on the electron microprobe. This method is not ideal for quantification, mostly due to the rough nature of the sample surfaces caused by quench texture (Figure 7A). It is difficult to determine what portion of a low electron microprobe analysis total is caused by surface heterogeneities as opposed to the presence of carbon, so it is assumed the entire deficit is from the presence of carbon. The previously shown Table 3 lists the carbon values for each run product found using this method, with the

average value and standard deviation for each composition. It should be noted that what is being called the amount of carbon in the run products is likely a combination of carbon and surface induced deficit. Experiments run above 6 GPa typically caused at least part of the graphite capsule to turn into diamond and this happened the most in the area directly surrounding the sample. Despite grinding these diamond capsule samples on diamond grinding discs, there still was a difference in relief between the diamond in the capsule and the sample surface. The relief made it difficult to create a well polished surface, which contributed to the low probe totals in some cases (Figure 7B). Most compositions show the average run product CO_2 content to be within one standard deviation of the ideal carbon content, so no density data points need to be removed due to anomalous amounts of carbon. Full microprobe analyses for all experiments are shown in Appendix A, along with information about microprobe data processing.

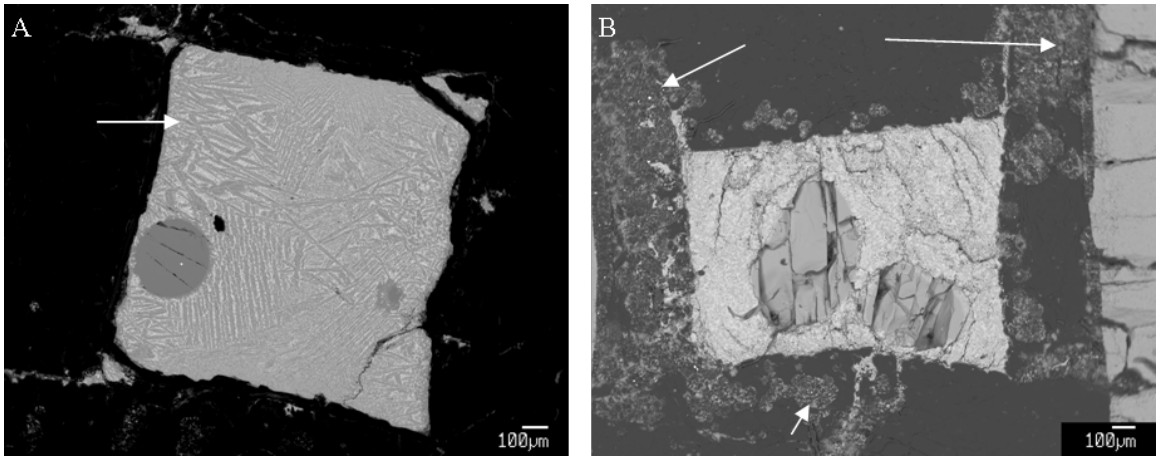

Figure 7: A: Sample C50-002, the white arrow shows a region of quench texture with particularly large quench crystals, but this texture can be seen throughout the entire sample area. B: Sample C100-010, white arrows show regions on the capsule that have turned to diamond. The diamondized regions are typically directly surrounding the sample area and make it difficult to create a smooth sample surface, which can also be seen in this image. Both images are BSE images.

The best dataset was obtained for the C50 composition in that neutral buoyancy and float results were obtained, allowing for a Birch-Murnaghan EOS fit. The other results did not give density brackets, but sink results can be used to determine an estimated region where the true compression curves for the melts lie, and the details of that process are described in the individual results sections about the different compositions. All one bar densities shown are calculated using the data of Lange and Carmichael (1987) and Liu and Lange (2003), and thus are not fixed values due to the uncertainty of these measurements. Liu and Lange (2003) measured 1 bar properties of carbonate liquids and determined that the mixing behavior between carbonate and silicate liquids is not linear, and thus it remains uncertain and is not able to be calculated accurately. The experimental results are compared with the Preliminary Reference Earth Model (PREM) of Dziewonski and Anderson (1981), which is a density model for the Earth derived from seismic data. This model gives an average density profile for the terrestrial mantle, and it should be noted that there are likely several regions in the mantle that deviate from this modeled density profile. Results for each composition will be discussed in their own section, then together to look at the effects of varying CO_2 content.

C100 Composition

The data for this composition are shown in Figure 8A. All results for this composition were sinks using Fo_{100} spheres. The sink results can be used to form a region showing where the true compression curve lies, and thus can provide a density maximum. Figure 8B shows this region (the shaded gray area), and shows one possible curve that fits the data obtained so far (dashed line). This curve is only an estimate, as it is not based on density brackets. Comparison of this data with PREM (Dziewonski and

Anderson 1981) shows at its maximum possible density, this melt could erupt from pressures up to 9 GPa on Earth (about 270 km).

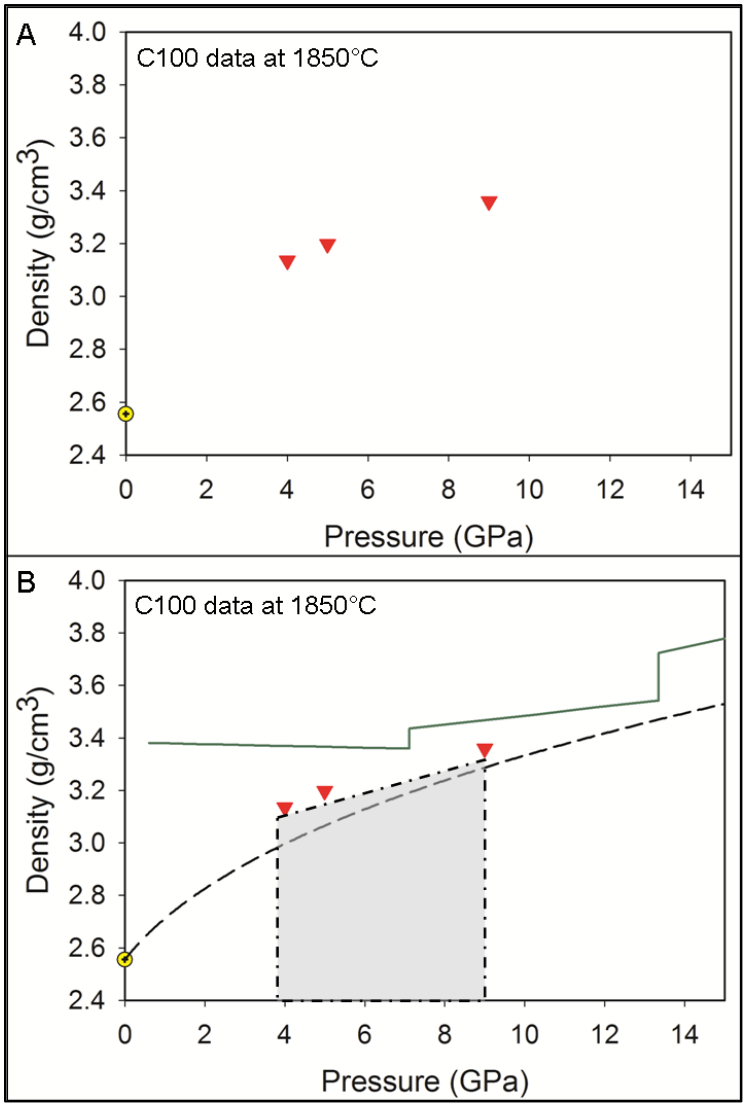

Figure 8: A: Experimental results from the C100 composition. B: C100 results plotted against PREM (Dziewonski and Anderson 1981), shown in green, to look for density crossovers. The shaded gray area shows the region where the compression curve for this melt lies; the dashed curve is an example of one curve that could fit the data obtained so far. Downward pointing red triangles are sink results, and the yellow circle at 0 GPa is the calculated one bar density for the melt using data from Lange and Carmichael (1987) and Liu and Lange (2003).

C50 Composition

This composition yielded the best results, which are shown in Figure 9A. Density brackets were determined with both Fo_{100} and Fo_{90} spheres, however the Fo_{90} float result is awaiting verification. These data were fitted to the Birch-Murnaghan equation, but since the compression behavior is only well constrained over the 5-10 GPa range, there are multiple solutions for the fit. Figure 9B shows the area where fitted curves would fall (shaded gray), the curves used to define that area, and their K_T, K', and 1 bar density parameters. The fitted curves are plotted against PREM (Dziewonski and Anderson 1981) for reference; the choice of K and K' greatly influence the shape of the curve and therefore the depths where this composition would be buoyant, and this figure emphasizes the uncertainty associated with extrapolating this data beyond the pressures at which it was derived. However, it highlights key pressures that would be useful to obtain density data at that could tighten the constraints on the curve with minimal experimentation. It should also be noted that the float result at 10 GPa needs verification because of heater failure during the run and the breakup of the capsule (resulting in loss of sample orientation) upon disassembly. The sample orientation was estimated using sphere dimension measurements, which are taken during experiment assembly. This experiment will be run again under the same conditions to verify the float result. The 10 GPa data point is critical as it shows a density crossover between the melt and PREM; data around 13 GPa would also be critical as there is a possibility of melt buoyancy past the 13 GPa discontinuity.

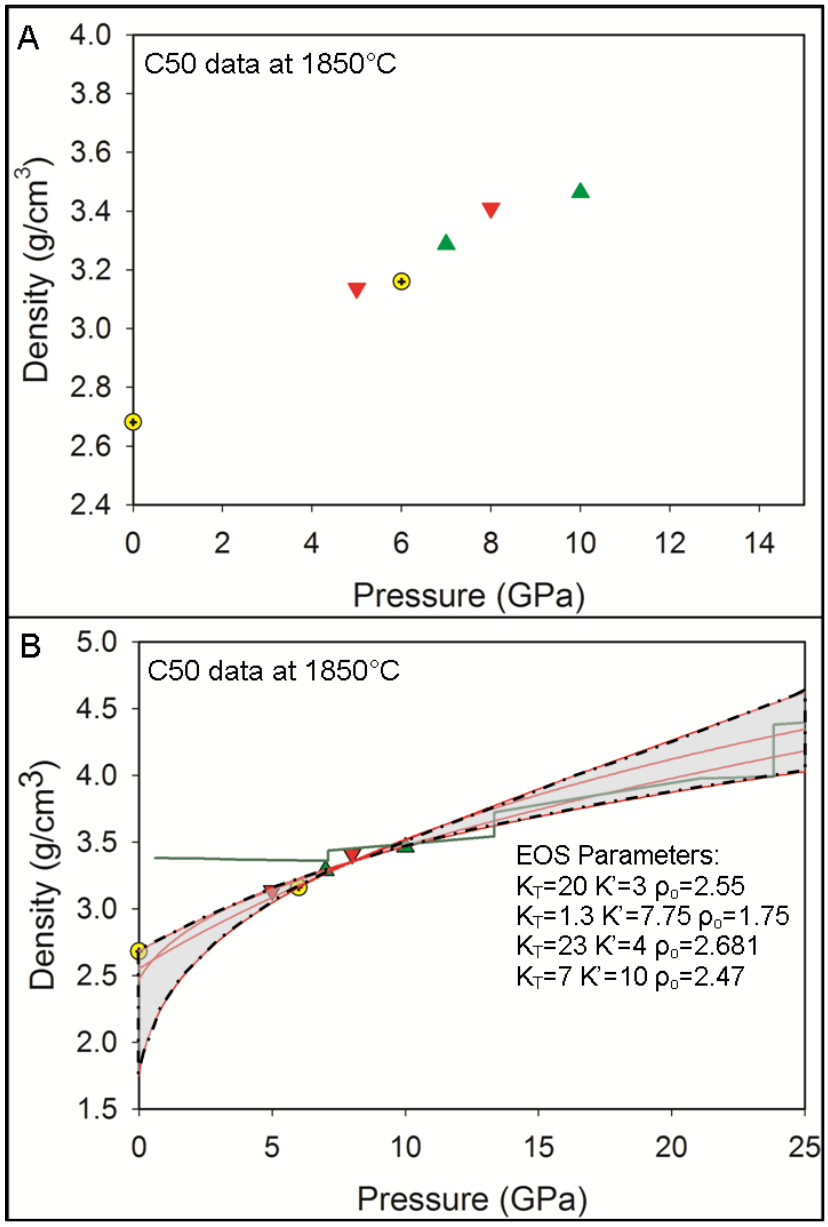

Figure 9: A: Experimental results from the C50 composition. The float result at 10 GPa needs verification due to experimental difficulties. B: C50 results plotted with PREM (Dziewonski and Anderson 1981), in green, to show density crossovers. The shaded gray region is the region where the true compression curve lies. The parameters for the curves that created the boundaries of this region (red curves on diagram) are also shown, K_T is in GPa and ρ_0 is in g/cm^3. Note the density crossover around 10 GPa is within the experimentally defined portion of the compression curve region. Downward pointing red triangles are sink results, upward pointing green triangles are float results, and the yellow circles are neutral buoyancy results. The neutral buoyancy at 0 GPa is the calculated one bar density for the melt using data from Lange and Carmichael (1987) and Liu and Lange (2003).

C25 Composition

The results for this composition are shown in Figure 10A. This composition is similar to the C100 composition in that only sink results were obtained. These results can be used to provide a maximum compression curve boundary line which shows the region where the actual compression curve is. An example compression curve is shown in Figure 10B. Comparing the data with PREM (Dziewonski and Anderson 1981) shows this melt is buoyant on Earth from pressures up to 9 GPa (around 270 km).

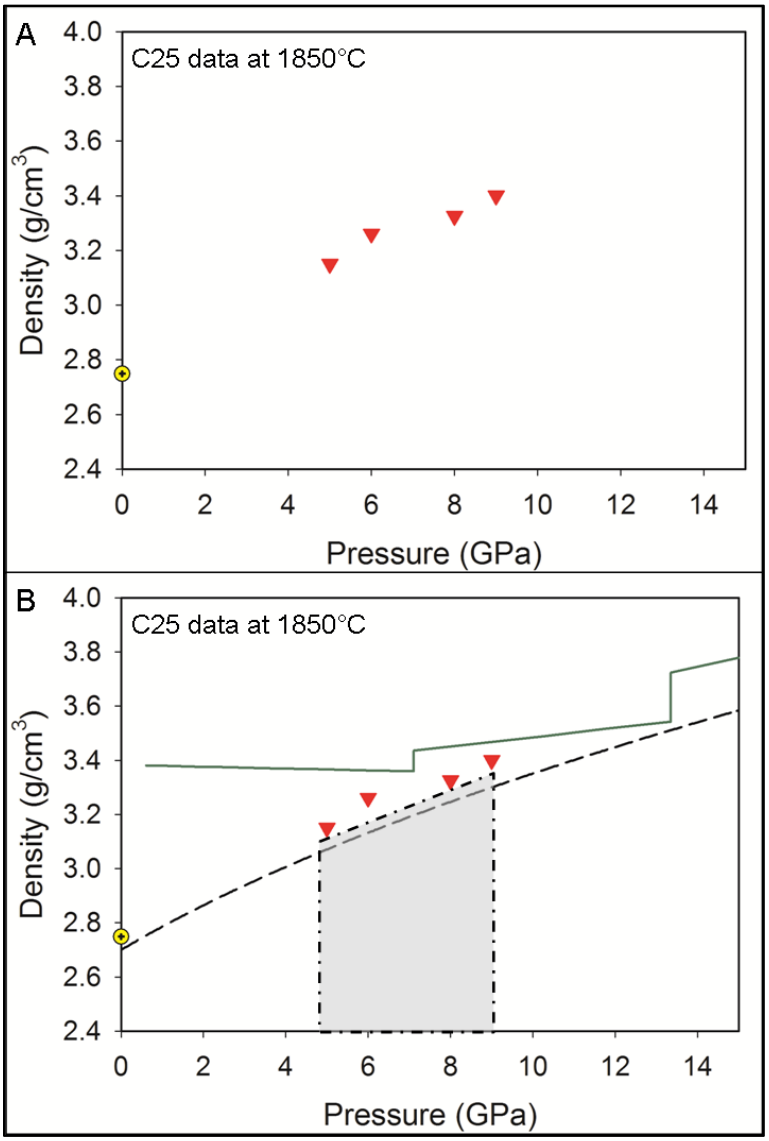

Figure 10: A: Experimental results for the C25 composition. B: The same results plotted with PREM (Dziewonski and Anderson 1981) shown in green for reference. The shaded gray area shows the region where the compression curve is. The dashed line shows one possible fit to the data so far. Based on this extrapolation, the C25 composition will have a density crossover with the C50 composition in the region of 8-11 GPa; this behavior is not shown in many of the previous carbonated melt density studies. Downward pointing red triangles are sink results, and the yellow circle at 0 GPa is the calculated one bar density for the melt using data from Lange and Carmichael (1987) and Liu and Lange (2003).

C0 Composition

Only two successful experiments were run for this composition, both giving sink results. As with C100 and C25, the data are shown in Figure 11A and the compression

curve region and an example fit to the data are shown in Figure 11B. The data show the melt to be buoyant up to 6 GPa (about 185 km).

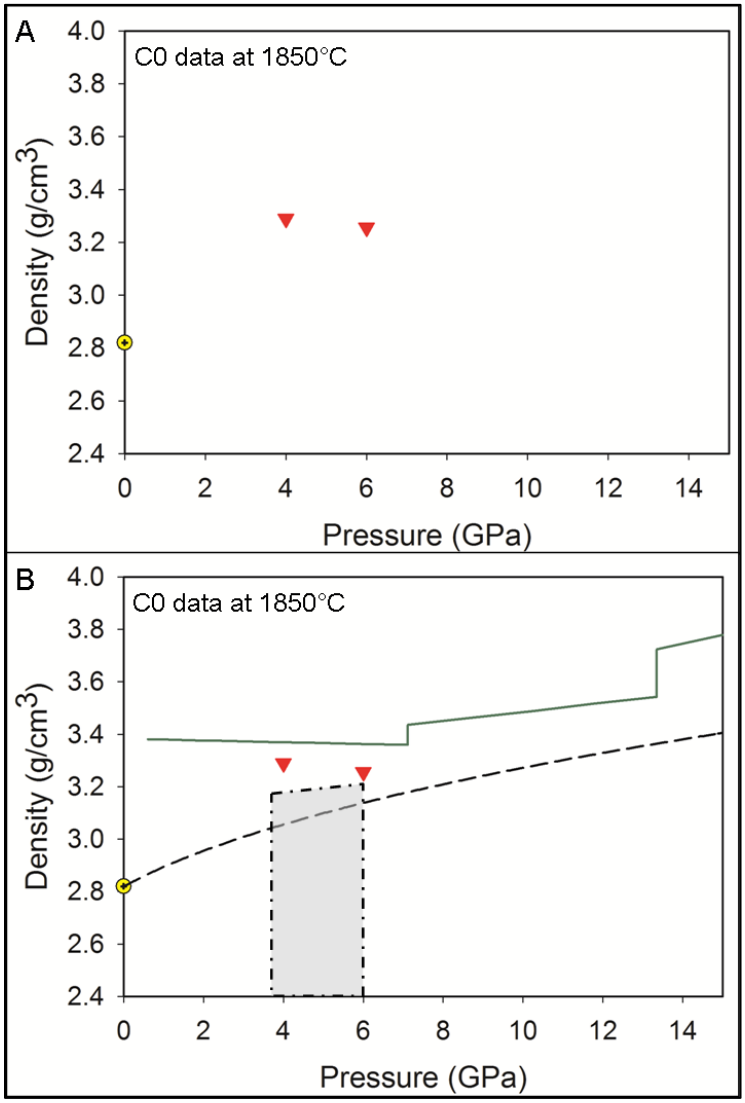

Figure 11: A: Experimental results for the C0 composition. B: The results plotted with PREM (Dziewonski and Anderson 1981), in green, for reference. The shaded gray region shows the area where the actual compression curve lies. The dashed curve is an example of a curve that fits the data obtained so far. Downward pointing red triangles are sink results, and the yellow circle at 0 GPa is the calculated one bar density for the melt using data from Lange and Carmichael (1987) and Liu and Lange (2003).

Collective Results

As few density brackets were found with these compositions, it is difficult to compare the exact effect of different amounts of CO_2 on the melt properties. It can be

seen that the different compositions have different densities, but we cannot yet determine the exact differences. As noted above, the data for the C25 and C50 compositions indicate a crossover between their compression curves in the region of 8-11 GPa. Many previous studies do not indicate such behavior (e.g. Ghosh et al. 2007, Sakamaki et al. 2011, Guillot and Sator 2011), and this crossover will have to be verified when more data for both compositions is obtained.

Discussion

Almost all of the experimental results from this study are sink results. The ideal results would have contained more density brackets to better fit compression curves to the data. However, as shown above, the sinks are still useful as they can give an upper limit to the melt density, which gives some insight into how CO_2 is affecting the density of these melts. These compositions are at the limit of the capabilities of the sink/float method as they have very low densities. Lower pressure melt density data cannot be obtained for these melts with this method because no minerals exist that are stable under the necessary run conditions with low enough densities and known equations of state. Thus experiments need to be run at higher pressures, but sink/float experiments are also limited in the high pressure regime due to capsule size constraints. Density studies on these compositions would benefit greatly by experiments run at a synchrotron beamline facility, where in situ density determinations would not be limited by the constraints associated with using mineral spheres.

The C0 composition appears to be refractory, and thus provided some difficulties for experiments. Many experiments on this composition failed to yield results because no spheres were found in the run products because they had melted during the experiment. This could be due to the temperatures used, or could be due to the spheres being

chemically unstable in the melt environment. But as they are Fo_{100} spheres and the melt is calculated by Kopylova et al (2007) to be in equilibrium with Fo_{95}, it is more likely that the spheres are melting. Some run products (C0-010 and C25-006) were found to only contain one sphere. This is likely caused by the thermal gradient in the capsule. The area in the center is hotter than the ends, and when spheres were moving, they passed through the center hot zone and melted. In all cases, the single sphere was found on the bottom of the capsule, so the results are either sinks or neutral buoyancies, and sinks are more consistent with the rest of the results.

Future Experimental Work

While this study has made progress on determining the effect of CO_2 on melt density for the chosen compositions, there is still more work to be done. Continued sink/float experimentation can be done on all the compositions to find further density brackets. Electron microprobe analyses to quantify carbon will be possible when a carbonate standard block is available. This can be useful for the IR analyses as well, as a carbon quantification can then be correlated with FTIR peak size and shape. As mentioned in the previous section, compositions such as these are at the limit of the sink/float method. Future work involving the use of a synchrotron facility for in situ density analyses will greatly enhance this dataset by providing low pressure data and data at pressures that are too high to successfully run sink/float experiments. While the synchrotron measurements will still be conducted at high pressure, they will allow for better constraints on the melt compression curve, which will allow better extrapolation back to the 1 bar melt density value. Better extrapolation to 1 bar melt densities will allow for better understanding of the mixing behavior between carbonate and silicate melts.

Further work in this area could also find the pressures where the melt compression curves for melts with different amounts of CO_2 have density crossovers with each other. This information would be valuable because it can show pressures where changing the melt composition can significantly change the density and therefore buoyancy path of the melt. With more CO_2 data, a more complete understanding of how CO_2 behaves in melts can then be combined with knowledge about H_2O in melts to see how the two behave together.

Chapter 3

Implications for Terrestrial Magmatism

Introduction

Sample analyses from the moon and Mars and surface analyses of Mercury indicate the interiors of these bodies are too reducing to produce large amounts of carbonated magmas (Papike et al. 2005, Hirschmann and Withers 2008, McCubbin et al. 2012). Currently there are no analyses to confirm the amount of carbonated volcanism on Venus, but based on observations it is likely some amount of carbonated volcanism has occurred there (see Chapter 4). Based on these observations, Earth has a relatively high occurrence of carbonated magmatism and volcanism compared to the other bodies in the inner Solar System. While CO_2 has been observed in almost all terrestrial magma types, it is of particular interest when it occurs in deeply generated magmas such as kimberlites. Kimberlites are enigmatic for many reasons, and the exact role of CO_2 in their origin and evolution is not well known. Further information about and application of how CO_2 effects melt density can be used to better understand these magmas and other deep Earth magmatic processes that cannot be directly observed.

Kimberlites

Kimberlites have been studied for many years due to their economic importance as the primary source for large, gem quality diamonds, and significant progress has been made regarding the petrogenesis of these magmas, however much remains unanswered. Kimberlites are not present in large volumes worldwide, but they are found in many different locations around the world and there are kimberlites on almost every continent (Keshav et al. 2005). It is thought that kimberlites travel relatively quickly to the surface and erupt explosively, however no kimberlite eruptions have been witnessed as they

range in age from late Precambrian to Cretaceous (Keshav et al. 2005). Despite many studies, there are still many points of controversy regarding kimberlites, particularly with regard to their origin.

Kimberlites are related to other silica undersaturated rocks such as melilitites, lamprophyres, and nephelinites (Keshav et al. 2005). They are silica undersaturated and have large amounts of volatiles, with H_2O and CO_2 as the primary volatile species (Sparks et al. 2009). Compositions from 388 kimberlites as referenced in Kjarsgaard et al. (2009) were examined to find data on typical kimberlite compositions and the results are listed in Table 6. The typical mineral assemblage for most kimberlites includes olivine, serpentine (from alteration), phlogopite, spinel, ilmenite, monticellite, igneous calcite, perovskite, and apatite (Sparks et al. 2009, Kopylova et al. 2007). There is some debate on whether kimberlites are formed from the mixing of refractory mantle material, such as harzburgite, with carbonate-rich fluid (e.g. Patterson et al. 2009) or are formed from the partial melting of carbonated mantle garnet lherzolite or carbonated peridotite (e.g. Gudfinnsson and Presnall 2005, Canil and Scarfe 1990). Melting experiments in the CMAS-CO_2 (CaO-MgO-Al_2O_3-SiO_2-CO_2) system produced kimberlite analogues over pressure ranges from 5-10 GPa (150-300 km) and only required less than 1% melting of the source material (Gudfinnsson and Presnall 2005). At lower temperatures of melting, carbonatite melts were produced and kimberlite melts were produced at higher temperature melting (Gudfinnsson and Presnall 2005). Mitchell (2004) conducted inverse method experiments using natural kimberlite material and found the kimberlite source to more likely be metasomatized mantle material, and that if this is the source material, then kimberlites form from greater than 1% melting of this source in the

pressure range of 5-12 GPa. A third possible formation mechanism was proposed by Russell et al. (2012) and states that carbonatites are the parent magma to kimberlites, and kimberlites are only formed if the carbonatite encounters orthopyroxene rich cratonic mantle lithosphere during ascent. Orthopyroxene was found to rapidly dissolve in carbonatite melts at 1 bar, which supports the lack of orthopyroxene found in kimberlite rocks, and this rapid assimilation causes rapid exsolution of a volatile phase, which decreases melt density and could be the mechanism that causes the rapid ascent of kimberlite magmas (Russell et al. 2012). If this is the source of kimberlite magmas, it can also explain the great diversity in kimberlite composition, as the amount of orthopyroxene assimilated is likely linearly related to distance travelled through cratonic mantle lithosphere, and also can explain the association of kimberlites with continents and specifically cratons (Russell et al. 2012). Evidence to support a deep source region for kimberlites is their association with high-pressure minerals and lithologies including garnet-bearing peridotite and diamonds (Keshav et al. 2005).

Table 6: The average, maximum, and minimum weight percents of major oxides in kimberlites. Note that not all original data was collected with the same method, some volatiles are reported based on loss on ignition values, and some studies report all iron in kimberlites as FeO. Data from Kjarsgaard et al. 2009.

	SiO_2	TiO_2	Al_2O_3	Fe_2O_3	FeO	MnO	MgO	CaO	Na_2O	K_2O	P_2O_5	H_2O	CO_2
Average	30.61	1.66	2.40	7.45	4.27	0.17	29.75	9.47	0.12	1.00	0.90	7.15	6.42
Maximum	38.53	5.66	4.45	16.99	9.00	0.56	39.75	23.76	0.52	3.62	5.58	13.67	15.10
Minimum	19.10	0.30	0.69	1.01	0.99	0.04	13.50	1.25	0.00	0.02	0.05	1.44	0.04
Standard Deviation	3.42	1.10	0.77	3.02	1.48	0.05	4.74	3.70	0.11	0.71	0.70	2.16	3.31

Application of Experimental Data

All experimental data from this study was plotted against PREM (Dziewonski and Anderson 1981) for reference in Figures 7B through 10B. The compositions with 12 and 3 wt% CO_2 do not exhibit density crossovers with PREM in the investigated pressure

range (up to 9 GPa). The composition with 0 wt% CO_2 does not show a density crossover up to 6 GPa. The 6 wt% CO_2 composition shows a density crossover with PREM at 10 GPa (around 300 km depth in the Earth). This implies that a kimberlitic magma with 6 wt% CO_2 as its only volatiles species cannot erupt if it is generated at pressures greater than 10 GPa (about 300 km). The density crossover is in a pressure region where the melt compression curve is directly defined by the experimental data, so it is not highly fit dependant, like the crossovers that occur in the gray shaded regions. What happens to the melt density at pressures above 10 GPa is uncertain, but further experiments in this pressure range will allow better constraints on the melt compression curve.

While many studies have focused on carbon dioxide in magma (e.g. Ghosh et al. 2007, Sakamaki et al. 2011, Duncan and Agee 2011), few have specifically focused on determining the density of kimberlitic magmas. The molecular dynamics study of Guillot and Sator (2011) did use a kimberlite composition free of water, and thus provides a good comparison to our dataset. Figure 12 shows our kimberlite densities plotted against those of Guillot and Sator (2011); data was compared based on amount of CO_2 and was normalized to 1850°C to remove differences due to temperature. Values for dK/dT (temperature derivative of the bulk modulus) were determined from Sakamaki et al. (2010) and Sakamaki et al. (2011) assuming dK/dT changed linearly with the addition of CO_2. The data of Guillot and Sator (2011) for kimberlites with 0, 2, and 10 wt% CO_2 falls in the shaded region determined from our data showing where the melt compression curves should lie for the 0, 3, and 12 wt% CO_2 compositions respectively. Our 6 wt% CO_2 composition and their 5 wt% CO_2 composition vary greatly, and it does not seem

likely that this variance is due to one extra weight per cent of CO_2. Our melt shows a more rapid increase in density, indicating it is more compressible over the pressure range shown. Since the C50 composition shows the most constraints on the compression curve, it is shown in Figure 13 with all of the kimberlite compression curves from Guillot and Sator (2011) and the proposed kimberlite source region is highlighted. At pressures above 5 GPa, our data do not fit any of the molecular dynamics derived compression curves. While the Guillot and Sator data show kimberlites to be able to erupt from the entire proposed source region (Gudfinnsson and Presnall 2005 and Mitchell 2004) if they contain anywhere from 0-10 wt% CO_2, our data show a kimberlite with 6 wt% CO_2 to be negatively buoyant above 10 GPa. This stark contrast may be highlighting a need for review of the parameters used in such molecular dynamics studies, and further experimental data can provide more insight. While the other three melts are in agreement with our data, it should be noted that we have the least constraints on the compression curves for these melts, and when more data become available, it is possible they will not agree with the data obtained from the molecular dynamics study. The deviation between our experimental data and the molecular dynamics data becomes apparent above 5 GPa, and this can set a lower limit for a pressure range that future studies should focus on when examining the effect of CO_2 on melt density. Also of note is the parallel shape of the Guillot and Sator (2011) compression curves. Most other carbonated melt compression curves don't show density crossovers between their carbonated and non-carbonated compositions, however some (e.g. Sakamaki et al. 2011, Ghosh et al. 2007) show non-parallel compression curves. Our data show a density crossover between the

C25 and C50 composition in the region of 8-11 GPa, which we would like to examine further with more experimental data.

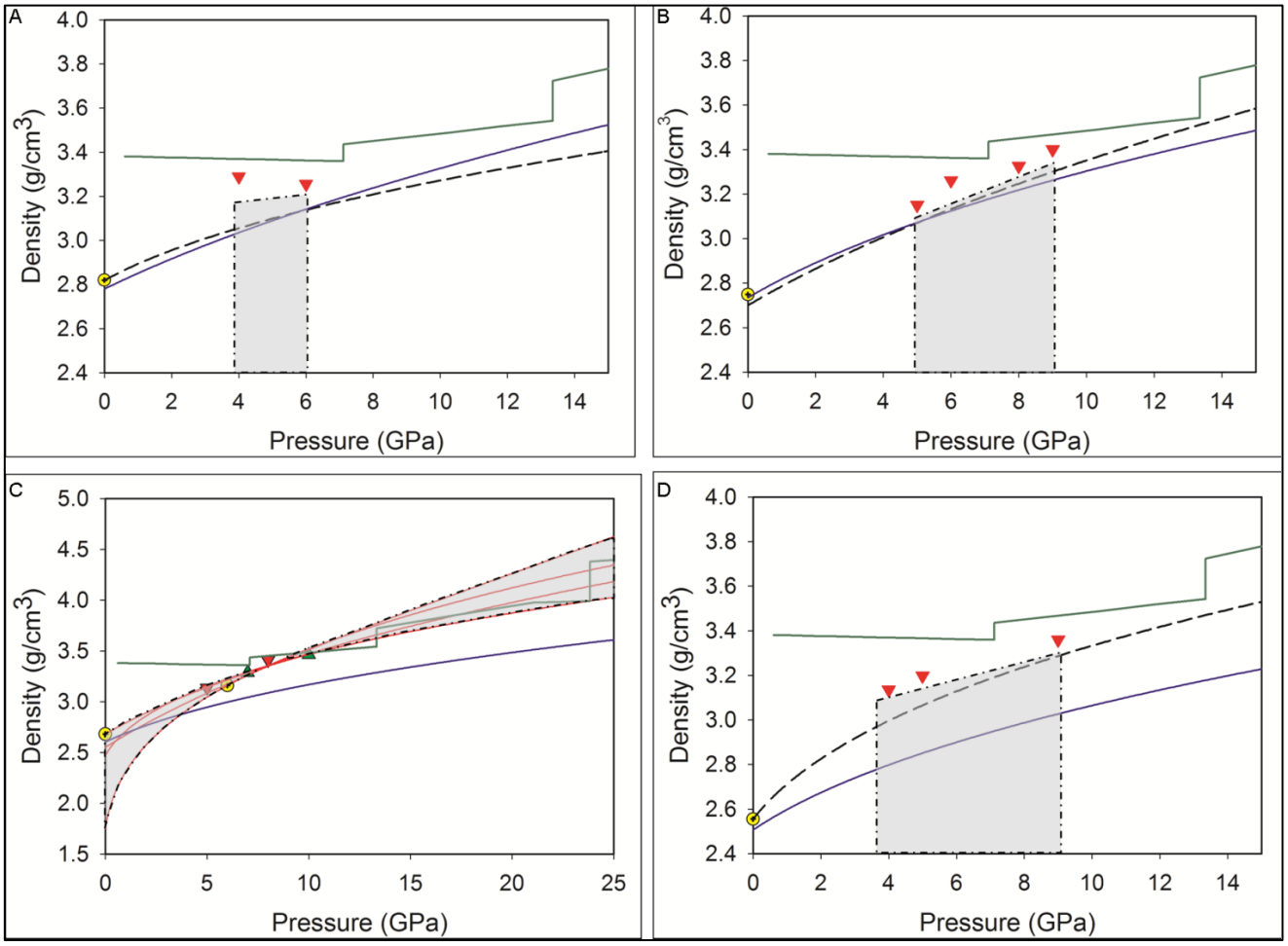

Figure 12: Experimental data from this study (similar to Figures 7B through 10B) plotted against kimberlite compression curves from Guillot and Sator (2011) normalized to 1850˚C. A: C0 vs. non-carbonated kimberlite. B: C25 vs. kimberlite with 2 wt% CO_2. C: C50 vs. kimberlite with 5 wt% CO_2. D: C100 vs. kimberlite with 12 wt% CO_2. The data from Guillot and Sator (2011) is shown in blue in each figure, and PREM (Dziewonski and Anderson 1981) is shown in green.

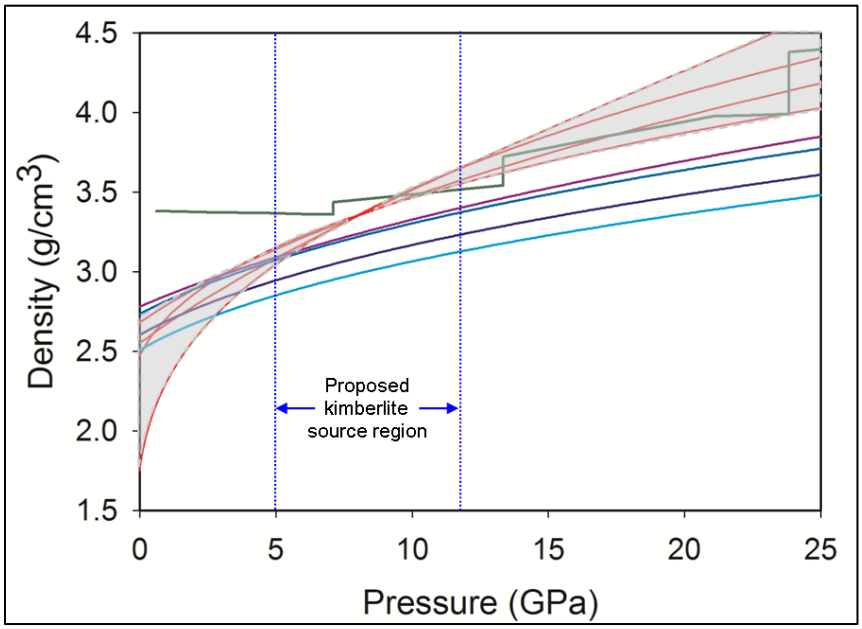

Figure 13: Plot of kimberlite densities from Guillot and Sator (2011) adjusted to 1850°C and the C50 composition from this study against PREM (Dziewonski and Anderson 1981, shown in green). The data from Guillot and Sator (2011) are as follows: light purple-0 wt% CO_2, dark blue-2 wt% CO_2, dark purple-5 wt% CO_2, light blue-10 wt% CO_2. The proposed kimberlite source region is bounded by the blue dotted lines and was determined from experiments by Gudfinnsson and Presnall (2005) and Mitchell (2004).

Based on our experimental data at this point, the C50 composition could be negatively buoyant at all pressures above 10 GPa, or it could only be negatively buoyant up to 13 GPa (around 380 km). These results show that a kimberlitic melt with 6 wt% CO_2 does not have a density restriction on its ability to erupt at pressures lower than 10 GPa, which supports the 5-10 GPa portion of the proposed source region from Gudfinnsson and Presnall (2005) and Mitchell (2004). If the compression curve does have another density crossover at 13 GPa, this indicates the possibility of carbonated melt ponding or cycling in the deep Earth. Melt ponding could potentially be a part of kimberlite genesis, as deep carbonated silicate melts could rise, become trapped and begin to crystallize, become enriched in volatiles due to removal of compatible elements, and then become buoyant again when they have a more kimberlitic composition.

Carbonated melt cycling could be what supplies volatiles and other incompatible elements from the deep earth to shallower mantle depths and keeps the whole mantle in communication chemically. Another possibility is that kimberlites could be deep carbonated melts that had anomalous volatile contents or passed through mantle regions with anomalous densities, allowing the melt to have the right density to be buoyant through the entire mantle, while melts with more typical volatile contents get trapped in the density driven cycle.

Chapter 4

Application to Venus

Introduction

While the thermoelastic data for melts determined from this and other studies can be applied to their respective compositions in any planetary mantle, Venus is the best candidate for the application of this data, aside from Earth, based on current knowledge. While the geologic dataset for Venus is relatively small compared to that of other inner solar system bodies (e.g. the moon, Mars), there is reason to believe its interior is oxidized enough for carbon to exist as C^{4+} at some depths, and therefore for carbonated magmas to be produced (e.g. Kargel et al. 1993, Elkins-Tanton et al. 2007). The interiors of the moon, Mars, and Mercury are too reducing for widespread existence of CO_2 in their mantles, as determined from sample analyses (Moon, Mars), surface analyses (Mercury), and core size estimates (Mercury) (Papike et al. 2005, Hirschmann and Withers 2008, McCubbin et al. 2012).

Evidence for Carbonated Magmatism

Based on the data we do have, the observed evidence for carbonated silicate magmas and carbonate magmas on Venus include the composition of the venusian atmosphere, the canali type channels, and thermodynamic calculations for calcite-anhydrite mixtures. The venusian atmosphere is around 96% CO_2 and is very dense, providing a surface atmospheric pressure of 95 bars (Taylor 1992, Barsukov 1992). As most components of planetary atmospheres are provided by magmatic volatiles, it is reasonable to assume this CO_2 was released from carbonated lavas generated in the planet's interior. The Magellan radar images of Venus showed a large number of channels on the surface, some of which appeared to be typical lava channels, but some

appeared to be formed by a low viscosity fluid due to their lengths, relatively constant widths along their entire length, and their smoothness (Baker 1997). The harsh surface conditions (95 bar atmospheric pressure and around 450°C average temperature) do not support liquid water, and it has been proposed that these canali type channels have been formed by low viscosity melts such as carbonatites and sulfur melts (Taylor 1992, Baker 1997). It was determined by Treiman (1995) using thermodynamic data that mixtures of calcite and anhydrite can be molten on the venusian surface only with added heat, likely provided by basaltic volcanism, or by melting point depression from the addition of alkali and halide elements. Both of these sources have been confirmed to be present on Venus at one time or another (Barsukov et al. 1992). These lines of evidence are based on surficial observations, and no directly obtained data exists for the venusian mantle. It is thought the venusian interior is largely similar to that of Earth with a major difference being the pressure gradient due to the slight difference in size between the planets (Barsukov et al. 1992, Taylor and McLennan 2009). Assuming the mantle mineralogy is the same between both planets, experimental data on carbonated peridotite and other mantle lithologies can be applied to Venus as well as Earth. The diagram in Figure 14 shows the solidus of carbonated and CO_2 free garnet lherzolite and highlights the P-T conditions required to form different magma types. If carbonated mantle lithologies exist on Venus as they do on Earth, these magmas will form under the same pressure and temperature conditions, but the depths of generation will be different. It has been determined by many experimental studies that carbonatitic and kimberlitic magmas are formed from small degrees of partial melting of carbonated mantle rocks such as peridotites (Canil and Scarfe 1990, Dalton and Presnall 1998a, Gudfinnsson and Presnall

2005). These lithologies are common in the terrestrial mantle, and would likely be common in the venusian mantle.

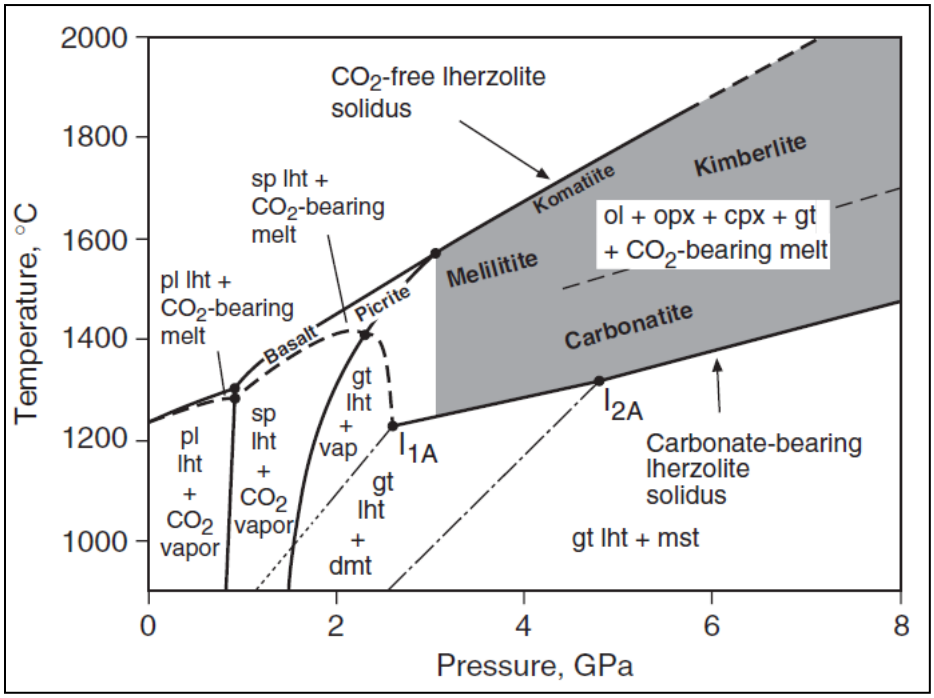

Figure 14: Diagram showing the solidi of carbonated and non-carbonated lherzolite. Regions of production for different types of melts, including kimberlites and carbonatites, are labeled. From Gudfinnsson and Presnall (2005) modified from Dalton and Presnall (1998a) and Presnall et al. (2002).

As stated previously, the correlation between pressure and depth is different for Venus than for Earth due to the slightly smaller radius of Venus. Because there is a difference in the pressure vs. depth trend, there is also a difference in mantle density vs. depth. The average mantle density profile for Earth (PREM) was determined by Dziewonski and Anderson (1981) from seismic data. Seismic data has not yet been obtained for Venus, and data such as core size (determined from moment of inertia) cannot be obtained due a lack of required data (Taylor and McLennan 2009). Some estimates of Venus mantle density profiles have been made based on what is known about Earth's mantle. The Parametrical Venus Model (PVM) is an Earth based model

using the terrestrial PEM-C model (Dziewonski et al. 1975) to determine density as a function of pressure and taking into consideration different amounts of iron in mantle silicates (Barsukov et al. 1992). These parameters were simplified into the PVM. Aitta (2012) used linear extrapolations from portions of PREM to approximate a density profile for the venusian mantle. For pressures up to 23.83 GPa, the terrestrial transition zone PREM linear dependence was used in the form of the equation $\rho(P)=3.2872+0.032775P$. For pressures above 23.83, the equation $\rho(P)=4.0578+0.014338P-2.3987*10^{-5}P^2$ describes the density-pressure relationship and is also based on PREM. Both models are shown in Figure 15 with PREM for reference. The major difference between the two Venus models is at pressures below 14 GPa, which are of interest to this study, due to density being purely a linear function of pressure in the Aitta model, whereas the PVM model follows PREM more closely and includes PREM's 13 GPa discontinuity in the form of a discontinuity at 14 GPa. The PVM model is preferred in this case, however it should be kept in mind that neither model is based on actual data from Venus and when such data becomes available the mantle density profile will likely change.

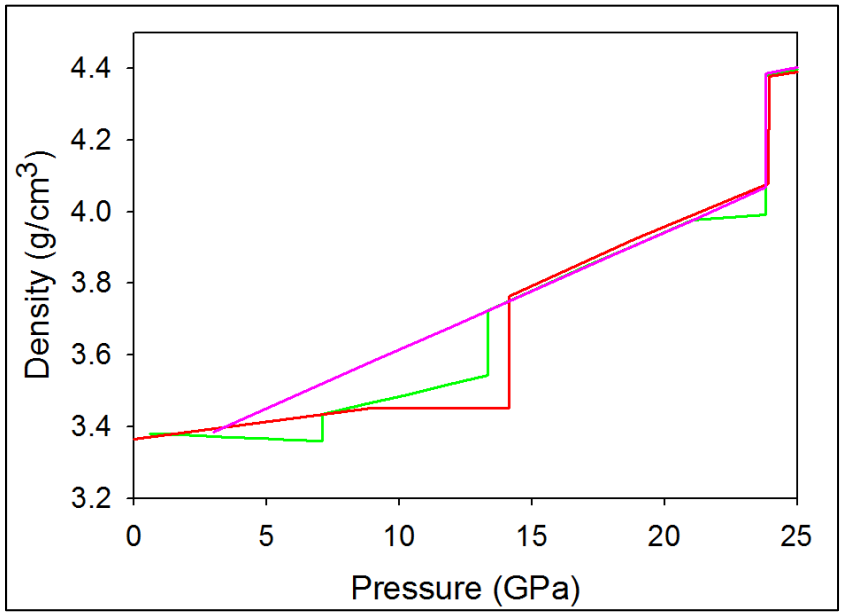

Figure 15: Comparison of mantle density models for Earth and Venus. The green line is PREM (Dziewonski and Anderson 1981), red line is PVM (Barsukov et al. 1992), and fuchsia line is the model of Aitta (2012).

Application of Melt Density Data

Just as melt density data can be applied to look for density crossovers in Earth's mantle, melt density data can be applied to Venus's mantle to find density crossovers. As our study only focused on kimberlitic melts, we used data from other carbonated melt studies (mentioned in Table 17) to examine a broader range of carbonated melt compositions. For the best comparison of different compositions, all the melt compression curves must be plotted at the same temperature, as temperature effects compressibility. This required using a dK/dT (temperature derivative of the bulk modulus) value for each melt. The peridotites of Sakamaki et al. (2010) and Sakamaki et al. (2011) have experimentally determined dK/dT parameters, and the chosen temperature of normalization is 1850°C, so the komatiite composition of Duncan and Agee (2011) did not have to be normalized. For both MORB compositions (Ghosh et al. 2007 and Guillot and Sator 2011), a dK/dT value for liquid hedenbergite from Lange (unpublished data)

was used because no MORB value was listed. The change in dK/dT between MORB with different amounts of CO_2 was scaled based on the change in dK/dT for peridotite with different amounts of CO_2 in the Sakamaki et al. (2010) and Sakamaki et al. (2011) papers.

Table 7: Thermoelastic parameters of melts used for comparisons with the Venus mantle. The Duncan and Agee data was derived at 1850°C and did not need to be corrected for temperature, so no dK/dT value is listed.

Composition (wt% CO_2)	Derivation Temperature (K)	K_T (GPa)	K'	dK/dT (GPa/K)	ρ_0 (g/cm^3)	Source
MORB (0)	2200	18.7	5	-0.0052*	2.59	Ohtani and Maeda 2001
MORB (5)	2300	17	5	-0.00801†	2.41	Ghosh et al. 2007
MORB (0)	2273	13.3	8.31	-0.0052*	2.59	Guillot and Sator 2011
MORB (2)	2273	11.2	9.66	-0.00632†	2.56	Guillot and Sator 2011
MORB (5)	2273	10.6	9.43	-0.00801†	2.5	Guillot and Sator 2011
Peridotite (0)	2100	24	7.3	-0.0027	2.7	Sakamaki et al. 2010
Peridotite (2.5)	1800	23	8.5	-0.01	2.65	Sakamaki et al. 2011
Komatiite (0)	1850	22.89	3.1	N/A	2.702	Duncan and Agee 2011
Komatiite (5)	1850	17.22	3.1	N/A	2.589	Duncan and Agee 2011

*-value from Lange (unpublished data) for liquid hedenburgite
†-calculated value using liquid hedenburgite from Lange (unpublished data) and percent difference between peridotite and carbonated peridotite from Sakamaki et al. 2010 and Sakamaki et al. 2011

The 1 bar melt densities of all the compositions were calculated at 1850°C using the same technique as for the kimberlitic melts, and the compression curves were plotted against the Venus mantle models (Figure 16A and 16C). Because the 1 bar densities of the CO_2 free MORBs used in the experimental studies (Ohtani and Maeda 2001, Ghosh et al. 2007, Guillot and Sator 2011) and the 1 bar density of the basalt analyzed by the Venera 14 mission (Barsukov et al. 1992) differ by about 0.02 g/cm^3, it is reasonable to apply the terrestrial MORB thermoelastic parameters to the venusian basalt. Thus the plotted basalts in Figure 16 are based on actual venusian basalt compositions. It should be noted that the data from Duncan and Agee (2011) has a K' value less than 4, which

results in large amounts of uncertainty when extrapolated beyond the pressure range from which the data was derived, therefore this data was plotted over the range of its derivation (4-6 GPa).

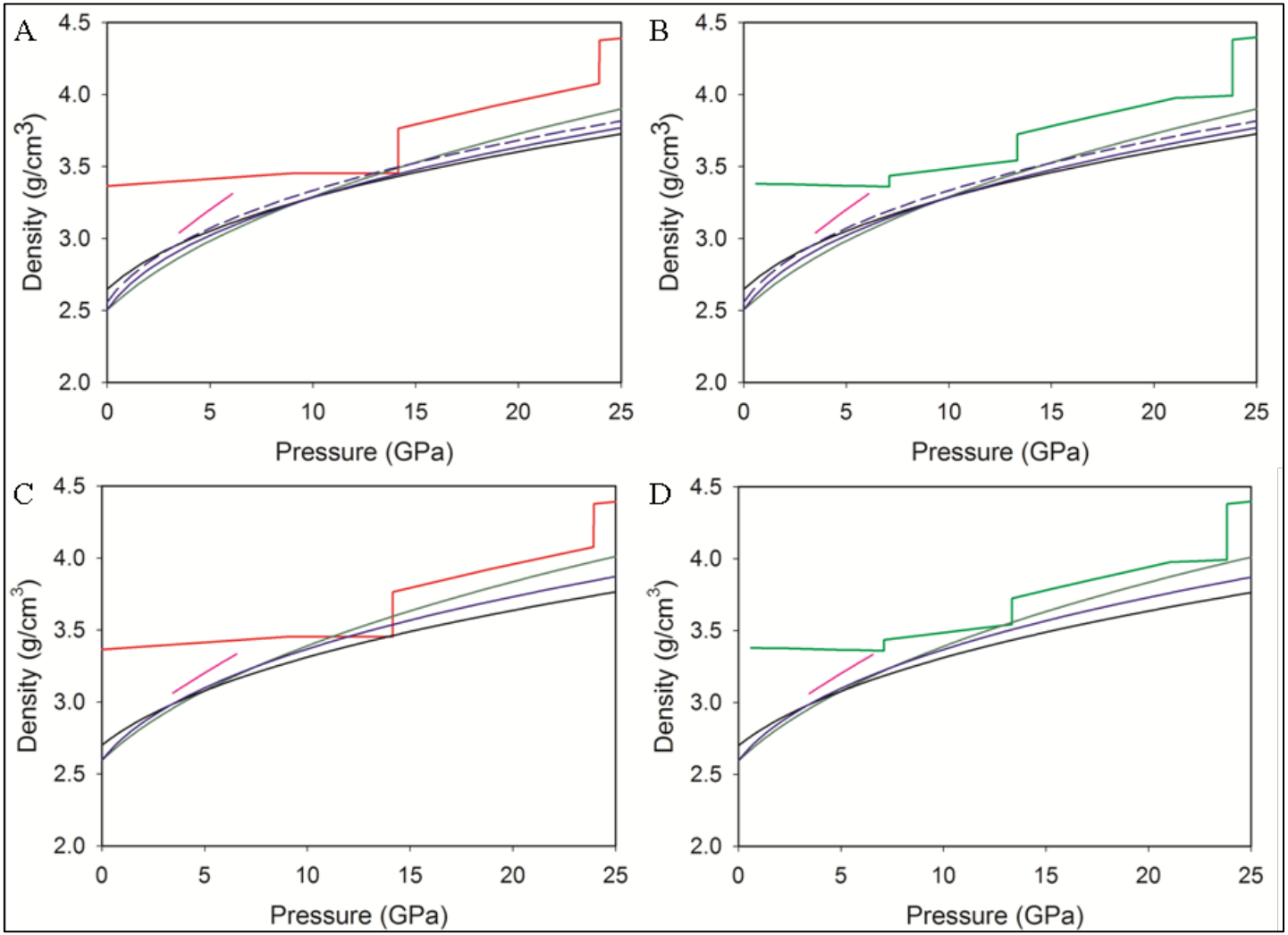

Figure 16: Melt compression curves plotted against PVM (red) and PREM (light green) (Barsukov et al. 1992 and Dziewonski and Anderson 1981). A and B show carbonated melt densities and C and D show non-carbonated melt densities. Dark green-MORB (carbonated from Ghosh et al. 2007, non-carbonated from Ohtani and Maeda 2001), Black-Peridotite (carbonated from Sakamaki et al. 2011, non-carbonated from Sakamaki et al. 2010), Fuchsia-komatiite from Duncan and Agee (2011), Blue-MORB from Guillot and Sator (2011), dashed blue-MORB with 2 wt% CO_2 from Guillot and Sator (2011).

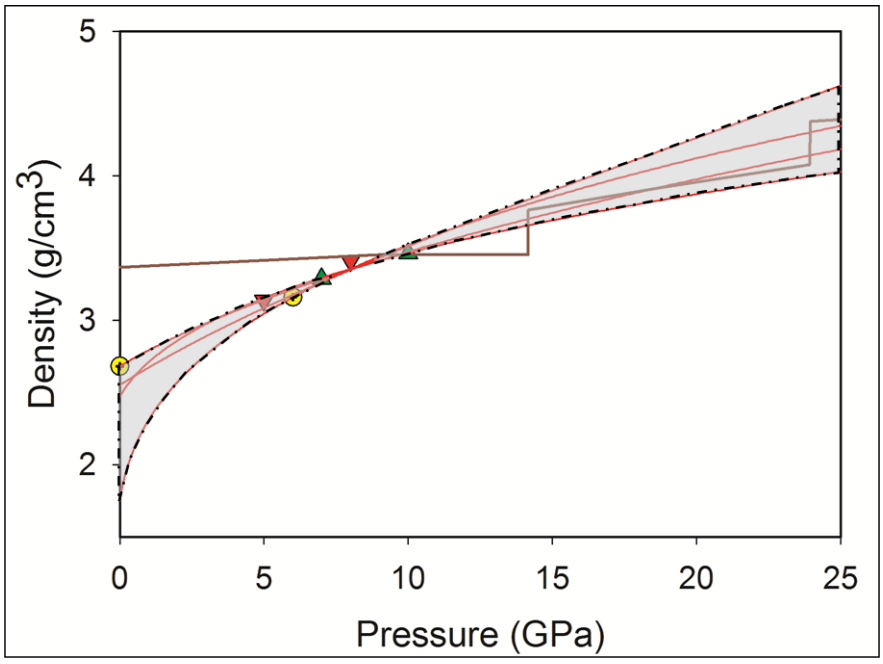

Figure 17: C50 results plotted against PVM (Barsukov et al. 1992). The mantle/melt density crossover occurs closer to 9 GPa in this model, extending the negative buoyancy region by 1 GPa.

Figure 16B and 16D also shows the same melts plotted against PREM for comparison between the two planets. All the carbonated melts can erupt from pressures up to 25 GPa on Earth, but only peridotite with greater than 2.5 wt% CO_2 and basalt with greater than 5 wt% CO_2 (based on Guillot and Sator 2011 data) can erupt from a similar pressure range on Venus. Similarly, the non-carbonated basalts from both studies can erupt from the entire pressure range shown on Earth, but could not erupt from above 14 GPa (around 480 km) on Venus. The C50 experiment data is plotted against PVM in Figure 17 for comparison to Figure 9. This composition shows a similar trend of having a lower pressure density crossover on Venus than on Earth. The shaded potential compression curve region does not show the intersection with PVM around 23.5 GPa that it has with PREM, meaning the melt could be buoyant at higher pressures than on Earth. The Venus mantle model is only an estimation, but based on this preliminary model, CO_2

is essential to have melts erupt from great depth on Venus. Due to the difference in pressure of density discontinuities between Earth's and Venus's mantles around 14 GPa, it is possible Venus has a larger region of trapped, ponding melts than Earth. The melts would be able to form and ascend from pressures above 14 GPa, but once they get to that pressure, there is a density crossover and they become negatively buoyant. This thicker layer of negatively buoyant or stalled melts could affect whole mantle processes on Venus such as convection and chemical homogeneity. The melt layer would essentially act as a second crust, storing incompatible elements at depth until the melt composition is altered through some process (i.e. fractional crystallization) that changes the melt density and allows it to leave the stalled melt zone.

When the surface of Venus can be extensively explored, it will be important to look for lithologies that contain mantle xenoliths to compare the deep mantle regions of Earth and Venus. Surface exploration of Venus will yield numerous valuable results and will allow for detailed geologic mapping and analyses, however it will likely be one of the most difficult planets to explore in this fashion. With advances in materials and technologies, a Venus deep seismic array would prove very useful as it could be deployed and data collection could occur with only the receivers remaining on the surface. Seismic data could tell us about the internal structure of the planet, the thickness of the crust, whether or not plate tectonics was ever active, and could detect molten material in the interior if it were present. With a ground truthed data set, a better model for the density of Venus's mantle could be created, and even without surface samples we could begin to assess melt eruptibility.

Appendices

Appendix A

Electron Microprobe Analysis

After microprobe data was collected, it was processed to obtain the average composition for each sample. Bad data points were removed before averaging according to the following method. Because an unknown portion of the deficit in the total is due to heterogeneous surface conditions, the analysis totals could not be used to determine bad data points. Instead, the data for the three most abundant oxides (SiO_2, MgO, and CaO) were used to determine bad points. The average weight percent of each element in each sample was determined, and any data point with values beyond one standard deviation from the average were eliminated. The totals for the remaining analyses were averaged and each oxide was normalized to the new average total to be able to better combine the analyses. Each oxide was then averaged, giving the composition of the sample. The total of these averaged oxides was used to determine the amount of carbon in the sample with the by difference method. Table A-1 shows the microprobe results for each sample in this study.

Table A-1: Electron microprobe analyses for all experiments. Values reported are oxide weight percents.

Experiment	C100-006	C100-007	C100-010	C0-006	C0-010
SiO_2	29.26	29.74	29.14	34.04	35.77
TiO_2	2.00	1.51	1.78	2.09	2.53
Al_2O_3	3.49	1.71	4.23	2.20	3.40
FeO	8.55	7.61	7.61	7.85	9.18
MgO	31.40	34.90	33.71	35.75	33.90
CaO	12.21	11.12	11.66	12.77	14.21
K_2O	1.07	0.68	0.12	0.33	0.21
CO_2	12.02	12.73	11.75	4.97	0.80

Experiment	C50-002	C50-003	C50-005	C50-007	C50-009
SiO_2	31.89	31.76	32.62	33.83	34.81
TiO_2	2.11	2.20	2.26	2.13	1.71
Al_2O_3	3.22	4.54	2.56	3.08	3.61
FeO	8.92	9.01	8.10	9.53	9.30
MgO	33.62	34.08	33.12	35.45	37.27
CaO	15.28	13.40	13.40	9.83	7.22
K_2O	0.15	0.17	0.14	0.10	0.06
CO_2	4.81	4.84	7.80	6.05	6.02

Experiment	C25-002	C25-003	C25-004	C25-006
SiO_2	33.00	33.77	34.89	34.44
TiO_2	2.11	2.11	2.17	1.86
Al_2O_3	2.83	2.75	3.43	2.30
FeO	8.74	8.75	8.97	7.69
MgO	35.25	35.28	36.48	36.70
CaO	16.07	12.72	9.86	10.58
K_2O	0.18	0.13	0.12	0.08
CO_2	1.82	4.49	4.08	6.35

Appendix B

Experiment Photos

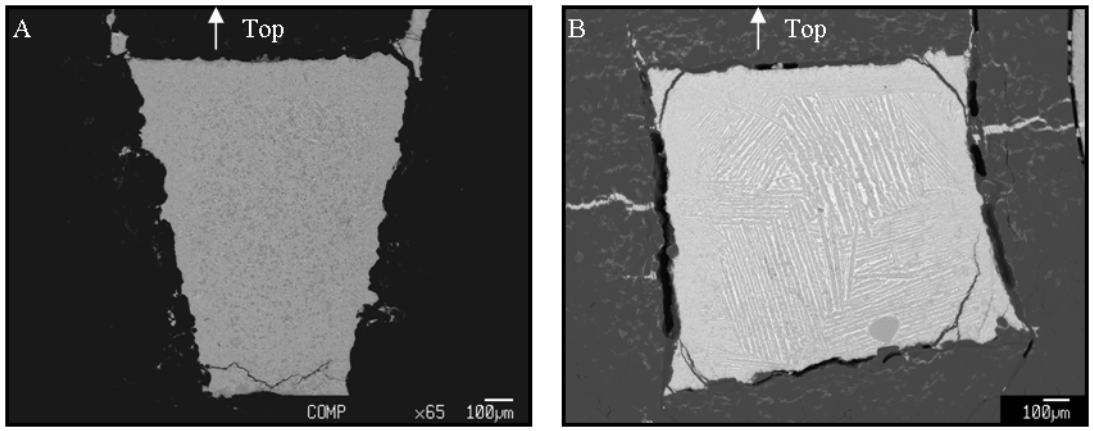

Figure B-1: BSE images of C0 experiments. A: C0-010, image in compositional mode. B: C0-006, image in compositional mode.

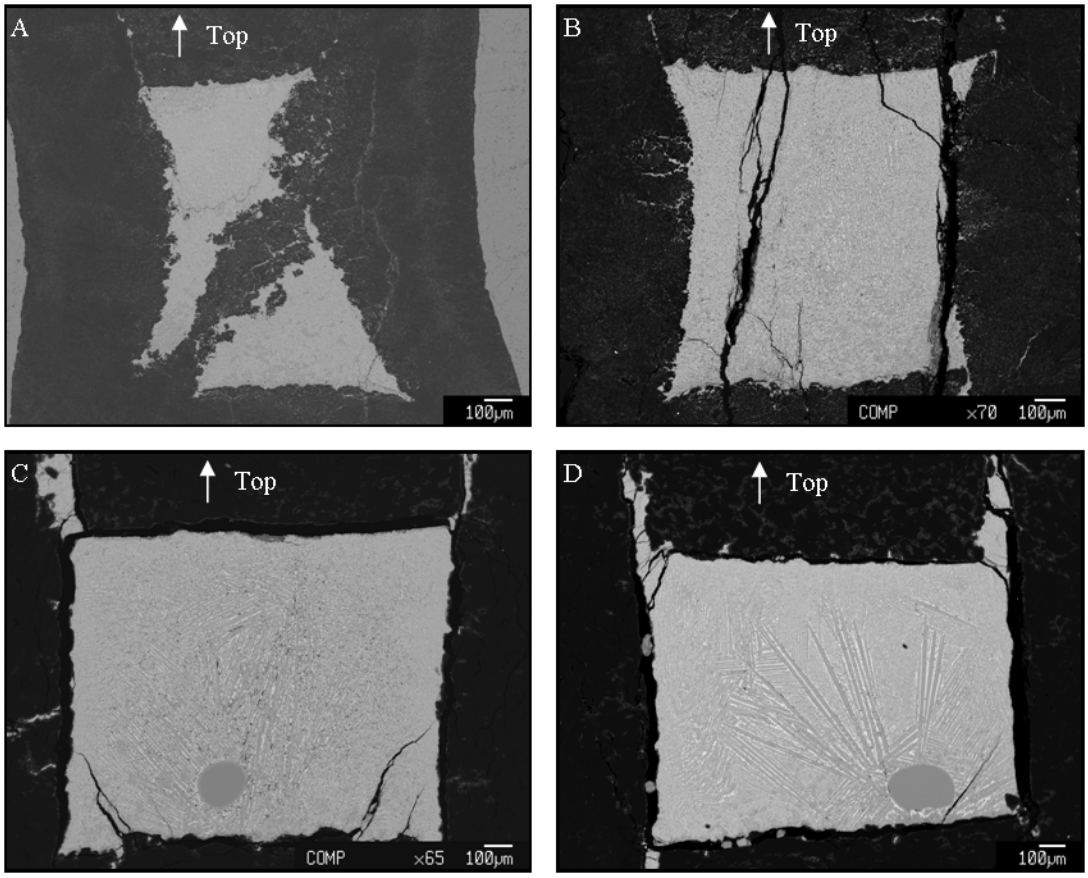

Figure B-2: BSE images of C25 experiments. A: C25-006 B: C25-004 C: C25-003 D: C25-002. All images are in compositional mode.

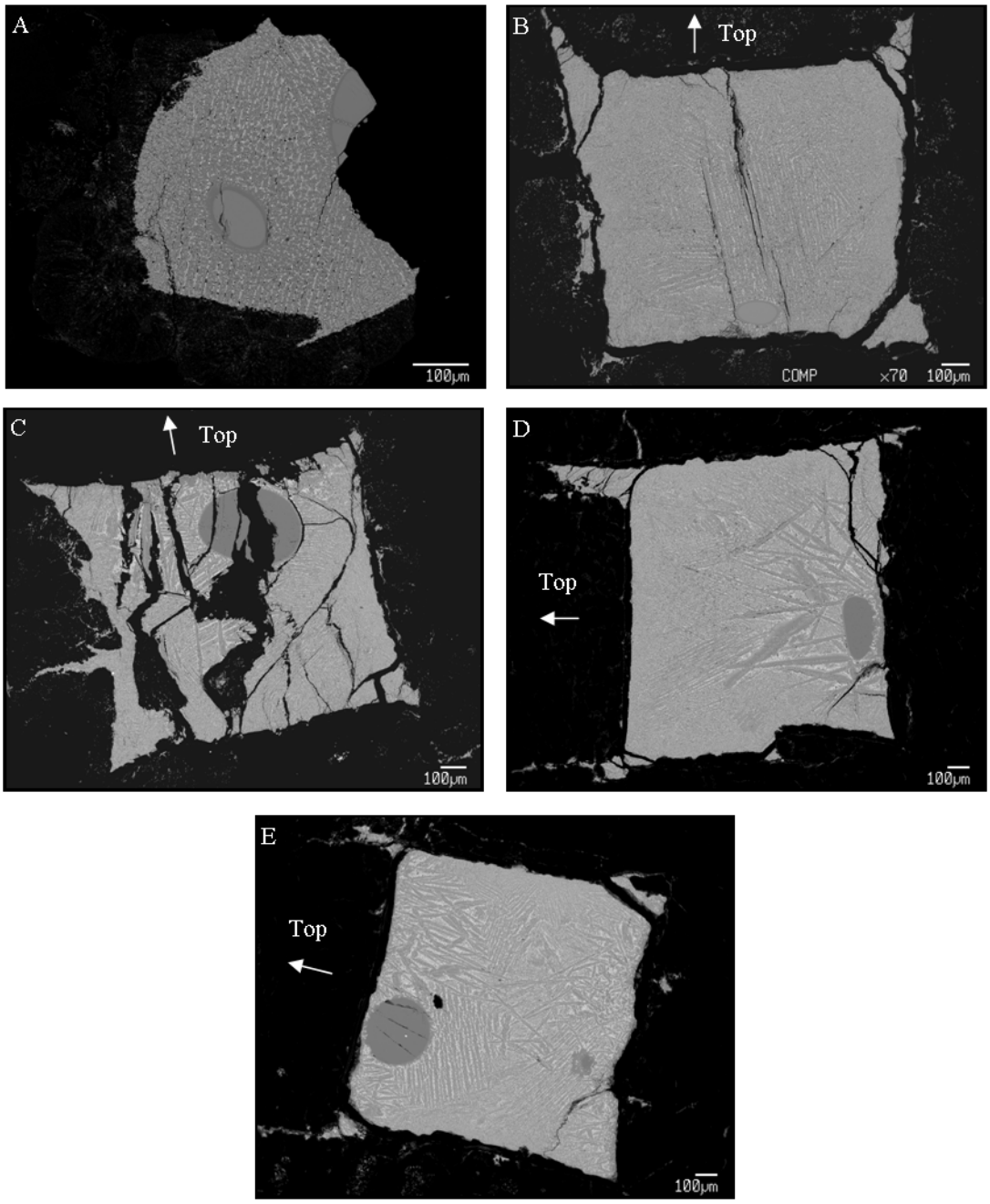

Figure B-3: BSE images of C50 compositions. A: C50-009, the capsule broke apart when being removed from the octahedron and sample orientation was lost. Based on sphere size measurements, the up direction appears to be the direction coming out of the page. Based on this data, the experiment was ruled a float, but needs to be verified. B: C50-007 C: C50-005 D: C50-003 E: C50-002. All images were taken in compositional mode.

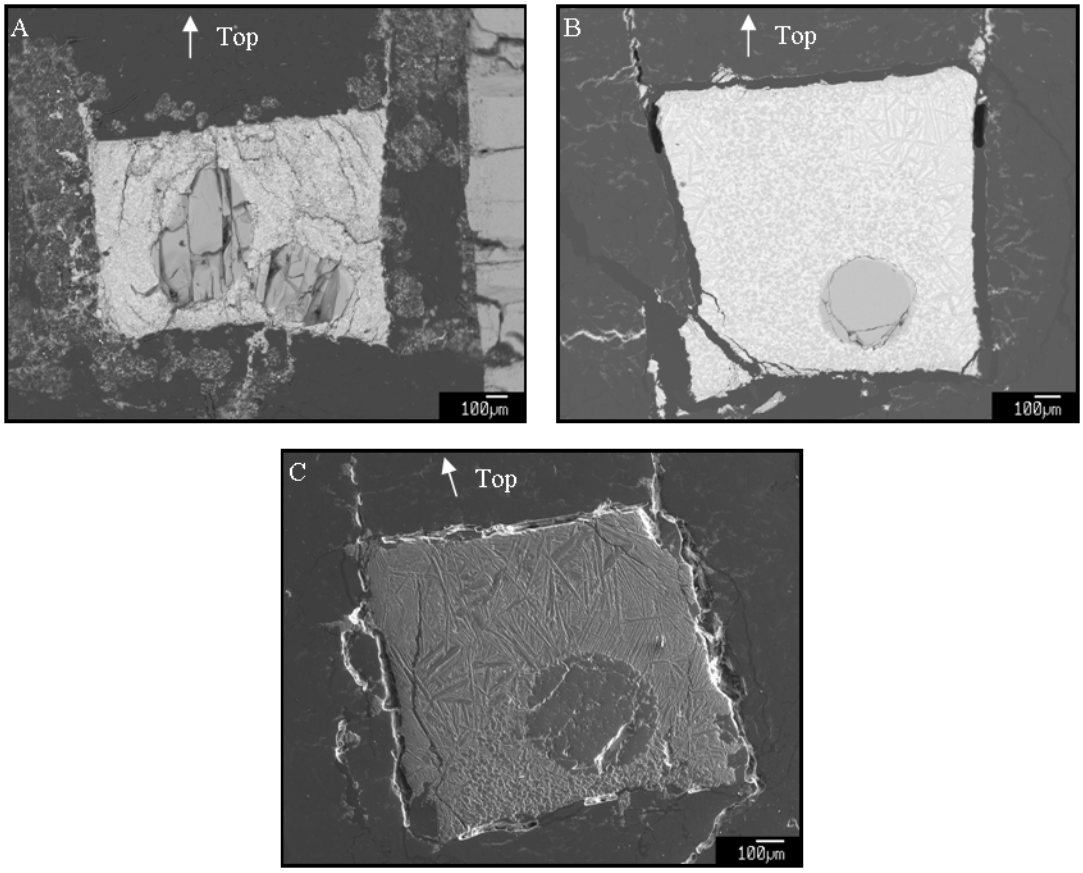

Figure B-4: BSE images of C100 experiments. A: C100-010, image in compositional mode. B: C100-007, image in SEI mode. C: C100-006, image in SEI mode.

Appendix C

Calculations

One bar densities for each melt were calculated for different applications. All 1 bar densities were found using data from Lange and Carmichael (1987) and Liu and Lange (2003). Any 1 bar density shown in this paper was calculated in this manner, including those shown in Figures 7-10, 11, 12, 15, and 16. For each experiment, the 1 bar density was used to correct the high pressure density for variations in composition of the run product and for temperature normalization. Examples of these processes are discussed here. After a sink/float run product is analyzed, the sphere density at the P-T conditions of the run is used as the base value for the melt density. When the sphere density is determined, the density value is then adjusted for changes in melt composition that occurred during the run. For example, if the run product contains more aluminum than the ideal composition, the 1 bar melt densities for the ideal and run product compositions are calculated, and the sphere density is offset by the difference between the two. This is essentially normalizing the density data to the ideal composition. Then in order to create an isothermal compression curve, the composition corrected densities are normalized to the same temperature. The 1 bar melt density of the composition being used is determined at the desired temperature, and the composition corrected densities are then corrected by the difference between this density and the 1 bar density at T of the experiment. Once all the density data for one composition is corrected for composition changes during the experiment and normalized to the same temperature, it can be plotted and the 3rd order Birch-Murnaghan equation can be fit to find a K_T and K' value.

Appendix D

Experimental Techniques Used to Determine Carbonated Melt Density

Sink/Float Method

The sink/float method (Agee and Walker 1988) involves using density markers with known equations of state to bracket the density of the material under investigation. The density markers are typically minerals with known equations of state such as olivine, garnet, and diamond (Agee and Walker 1988, van Kan Parker et al. 2011, Ghosh et al. 2007). The density markers are made from gem quality crystals that are broken into small fragments and ground into spheres using the Bond air mill (Bond 1951). Experiments use two density markers if capsule size allows, but can also be run with one density marker if needed (e.g. Ghosh et al. 2007). The density markers are loaded into the capsule so that one begins near the top and one begins near the bottom (Figure 4). The mineral spheres should be placed so that they are not in contact with the capsule walls to minimize the risk of the spheres sticking to the walls during the run.

Once the experiment is at the desired P-T conditions, the sample material should be molten and the density markers are free to move in the capsule due to buoyancy. The possible movements of the markers and related results are shown in the bottom of Figure 4. If the markers are more dense than the sample (melt), they sink to the bottom. If the markers are less dense than the sample, they float to the top. If the markers and sample are the same density, the markers remain in their starting positions. The results are deemed a sink, float, and neutral buoyancy respectively. Since the density markers have known equations of state, their densities at the experimental conditions are known. The results are plotted on a density vs. pressure diagram (after the corrections discussed in Appendix C), and a compression curve can be fit to the data. Sink results and float

results from the same density marker create a bracket showing where the actual sample density is, and the more brackets that are determined, the better the fit of the compression curve. Neutral buoyancy results allow the determination of the melt density (equal to the density marker density), but these results must be verified to be certain the sample material melted completely and there was no other reason the markers didn't move. This method has been verified by several studies on carbonated and non-carbonated melts alike (Agee and Walker 1988, van Kan Parker et al. 2011, Duncan and Agee 2011, Ghosh et al. 2007).

X-Ray Absorption Method

The X-ray absorption method for determining melt density is an in situ technique, as it involves making measurements when the experiment is at the P-T conditions of interest. These experiments must be conducted at beamline facilities, as the beamline is the source of the X-rays. The X-ray absorption studies of interest here are those of Sakamaki et al. (2010) and Sakamaki et al. (2011). Diamond capsules were used for the experiments to minimize the capsule distortion during the run and to allow the X-rays to penetrate the sample material. The X-ray intensity is measured before and after passing through the sample, and these intensities along with other parameters are used to find the sample density according to the following equation:

$$\rho_{sample} = \frac{-1}{2\mu_{sample} t(x)} \frac{\ln I(x)_{sample} - \ln I(x)_{diamond}}{\ln I_0\,(x)_{sample} - \ln I_0\,(x)_{diamond}} + \mu_{diamond}\rho_{diamond}$$

where ρ_{sample} is the sample density, μ_{sample} is the mass absorption coefficient of the sample, I is the X-ray intensity before absorption, I_0 is the intensity after absorption, x is the sample position, $\mu_{diamond}$ is the mass absorption coefficient for diamond, and $\rho_{diamond}$ is the density of diamond. The density of diamond is determined from an equation of state.

The mass absorption coefficients used in this study were assumed to be independent of pressure and temperature and to only depend on X-ray energy and atomic number. This parameter was measured for both diamond and the sample under ambient conditions (while density and thickness are known), and was assumed to be the same when at experimental conditions.

Molecular Dynamics Simulations

The molecular dynamics study of interest to this paper is that of Guillot and Sator (2011). Molecular dynamics (MD) simulations involve iterative solving of equations of motion for a given amount of particles interacting using a given force field (Guillot and Sator 2011). This simulation was run to show the equilibration of a silicate melt with a supercritical CO_2 fluid phase at given pressure and temperature conditions, and accounts for the reaction between CO_2 molecules and the melt (reaction according to: $CO_2+(O^{2-})_{melt}<=>(CO_3^{2-})_{melt}$). The simulation requires interaction parameters to describe the interactions between the CO_2 fluid and silicate melt (CO_2-CO_2 interaction, CO_2-silicate interaction, silicate-silicate interactions), and the accuracy of these parameters greatly influences the accuracy of the simulation. The details of the derivation of these parameters and the workings of the model are beyond the scope of this study.

References

Agee, C. B. and D. Walker. (1988) Static compression and olivine flotation in ultrabasic silicate liquid. *Journal of Geophysical Research*. **93**: 3437-3449.

Aitta, A. (2012) Venus' internal structure, temperature and core composition. *Icarus*. **218**: 967-974.

Baker V. R., G. Komatsu, V. C. Gulick, and T. J. Parker et al. (1997) Channels and valleys, in *Venus II* (eds. S.W. Bougher, D.M. Hunten, and R.J. Phillips), University of Arizona Press pp. 757-793.

Barsukov, V. L., A. T. Basilevsky, V. P. Volkov, and V. N. Zharkov (eds.) (1992) *Venus Geology, Geochemistry, and Geophysics.* University of Arizona Press, Tucson, p. 421.

Birch, F. (1952) Elasticity and constitution of the earth's interior. *Journal of Geophysical Research*. **57**: 227-286.

Bond, W. L. (1951) Making small spheres. *Review of Scientific Instruments*. **22**: 344-345.

Canil, D. and C. M. Scarfe. (1990) Phase relations in peridotite+CO_2 systems to 12 GPa: Implications for the origin of kimberlite and carbonate stability in the Earth's upper mantle. *Journal of Geophysical Research*. **95**: 15805-15816.

Dalton, J. A. and D. C. Presnall. (1998) Carbonatitic melts along the solidus of model lherzolite in the system CaO-MgO-Al_2O_3-SiO_2-CO_2 from 3 to 7 GPa. *Contributions to Mineralogy and Petrology*. **131**: 123-135.

Dobson, D. P., A. P. Jones, R. Rabe, T. Sekine, K. Kurita, T. Taniguchi, T. Kondo, T. Kato, O. Shimomura, and S. Urakawa. (1996) In-situ measurement of viscosity and density of carbonate melts at high pressure. *Earth and Planetary Science Letters*. **143**: 207-215.

Duncan, M. S., and C. B. Agee. (2011) The partial molar volume of carbon dioxide in peridotite partial melt at high pressure. *Earth and Planetary Science Letters*. **312**: 429-436.

Dziewonski, A. M., A. L. Hales, and E. R. Lapwood. (1975) Parametrically simple Earth models consistent with geophysical data. *Physics of the Earth and Planetary Interiors*. **10**: 12-48.

Dziewonski, A. M. and D. L. Anderson. (1981) Preliminary reference Earth model. *Physics of the Earth and Planetary Interiors*. **25**: 297-356.

Eggler, D. H. and M. Rosenhauer. (1978) Carbon dioxide in silicate melts. II. Solubility of CO_2 and H_2O in $CaMgSi_2O_6$ (diopside) liquids and vapors at pressures to 40 kb. *American Journal of Science*. **278**: 64-94.

Elkins-Tanton, L. T., S. E. Smrekar, P. C. Hess, and E. M. Parmentier. (2007) Volcanism and volatile recycling on a one-plate planet: Applications to Venus. *Journal of Geophysical Research*. **112**, E04S06.

Genge, M. J., G. D. Price, and A. P. Jones. (1995) Molecular dynamics simulations of $CaCO_3$ melts to mantle pressures and temperatures: Implications for carbonatite magmas. *Earth and Planetary Science Letters*. **131**: 225-238.

Ghosh, S., E. Ohtani, K. Litasov, A. Suzuki, and T. Sakamaki (2007), Stability of carbonated magmas at the base of the Earth's upper mantle, *Geophysical Research Letters*, **34**, L22312, doi:10.1029/2007GL031349.

Graham E. K., J. A. Schwab, S. M. Sopkin, and H. Takei (1988) The pressure and temperature-dependence of the elastic properties of single-crystal fayalite Fe_2SiO_4. *Physics and Chemistry of Minerals.* **16,** 186-198.

Gudfinnsson, G. H. and D. C. Presnall. (2005) Continuous gradations among primary carbonatitic, kimberlitic, melilititic, basaltic, picritic, and komatiitic melts in equilibrium with garnet lherzolite at 3-8 GPa. *Journal of Petrology*. **46**: 1645-1659.

Guillot, B. and N. Sator. (2011) Carbon dioxide in silicate melts: A molecular dynamics simulation study. *Geochimica et Cosmochimica Acta*. **75**: 1829-1857.

Harris, M., A. le Roex, and C. Class. (2004) Geochemistry of the Uintjiesberg kimberlite, South Africa: petrogenesis of an off-craton, group I, kimberlite. *Lithos*. **74**: 149-165.

Hazen R. M. (1997) Effects of temperature and pressure on crystal-structure of ferromagnesian olivine. *American Mineralogist.* **62,** 286-295.

Hirschmann, M. M. and A. C. Withers. (2008) Ventilation of CO_2 from a reduced mantle and consequences for the early Martian greenhouse. *Earth and Planetary Science Letters*. **270**:147-155.

Isaak D. G., E. K. Graham, J. D. Bass, and H. Wang (1993) The elastic properties of single-crystal fayalite as determined by dynamical measurement techniques. *Pure and Applied Geophysics.* **141:** 393-414.

Jacobs M. H. G. and B. de Jong (2007) Placing constraints on phase equilibria and thermophysical properties in the system MgO-SiO_2 by a thermodynamically consistent vibrational method. *Geochimica Cosmochimica Acta,* **71:** 3630-3655.

Kargel, J. S., G. Komatsu, V. R. Baker, and R. G. Strom. (1993) The volcanology of Venera and VEGA landing sites and the geochemistry of Venus. *Icarus*. **103**: 253-275.

Keshav, S., A. Corgne, G. H. Gudfinnsson, M. Bizimis, W. F. McDonough, and Y. Fei. (2005) Kimberlite petrogenesis: Insights from clinopyroxene-melt partitioning experiments at 6 GPa in the CaO-MgO-Al_2O_3-SiO_2-CO_2 system. *Geochimica et Cosmochimica Acta*. **69**: 2829-2845.

Kjarsgaard, B. A., D. G. Pearson, S. Tappe, G. M Nowell, and D. P. Dowall. (2009) Geochemistry of hypabyssal kimberlites from Lac de Gras, Canada: Comparisons to a global database and applications to the parent magma problem. *Lithos*. **112S**: 236-248.

Klein-BenDavid, O., E. S. Izraeli, E. Hauri, and O. Navon. (2004) Mantle fluid evolution-a tale of one diamond. *Lithos*. **77**: 243-253.

Kopylova, M. G., S. Matveev, and M. Roudsepp. (2007) Searching for a parental kimberlite melt. *Geochimica et Cosmochimica Acta*. **71**: 3616-3629.

Lange, B. A. and I. S. E. Carmichael. (1987) Densities of Na_2O-K_2O-CaO-MgO-FeO-Fe_2O_3-Al_2O_3-TiO_2-SiO_2 liquids: new measurements and derived partial molar properties. *Geochimica et Cosmochimica Acta*. **51**: 2931-2946.

Le Roex, A. P. and M. Becker. (2006) Geochemistry of South African on-and off-craton, Group I and Group II kimberlites: Petrogenesis and source region evolution. *Journal of Petrology*. **47**: 673-703.

Liu, Q. and R. A. Lange. (2003) New density measurements on carbonate liquids and the partial molar volume of the $CaCO_3$ component. *Contributions to Mineralogy and Petrology*. **146**: 370-381.

Liu, W. and B. S. Li (2006) Thermal equation of state of $(Mg_{0.9}Fe_{0.1})_2SiO_4$ olivine. *Physics of the Earth and Planetary Interiors.* **157:** 188-195.

McCubbin, F. M., M. A. Riner, K. E. Vander Kaaden, and L. K. Burkemper. Is Mercury a volatile-rich planet? *Geophysical Research Letters*. **39**: L09202, doi:10.1029/2012GL051711.

Mitchell, R. H. (1997) *Kimberlites, Orangeites, Lamproites, Melilitites, and Minettes: A Petrographic Atlas*. Almaz Press Inc., Ontario, Canada, pp. 243.

Mitchell, R. H. (2004) Experimental studies at 5-12 GPa of the Ondermatjie hypabyssal kimberlite. *Lithos*. **76**: 551-564.

Ohtani, E., and M. Maeda. (2001) Density of basaltic melt at high pressure and stability of the melt at the base of the lower mantle. *Earth and Planetary Science Letters*. **193**: 69-75.

Papike, J. J, J. M. Karner, and C. K. Shearer. (2005) Comparative planetary mineralogy: Valence state partitioning of Cr, Fe, Ti, and V among crystallographic sites in olivine, pyroxene, and spinel from planetary basalts. *American Mineralogist*. **90**: 277-290.

Patterson, M., D. Francis, and T. McCandless. (2009) Kimberlites: magmas or mixtures? *Lithos*. **112S**: 191-200.

Presnall, D. C., G. H. Gudfinnsson, and M. J. Walter. (2002) Generation of mid-ocean ridge basalts at pressures from 1 to 7 GPa. *Geochimica et Cosmochimica Acta*. **66**: 2073-2090.

Russell, J. K., L. A. Porritt, Y. Lavallée, D. B. Dingwell. (2012) Kimberlite ascent by assimilation-fuelled buoyancy. *Nature*. **481**: 352-356.

Sakamaki, T., E. Ohtani, S. Urakawa, A. Suzuki, and Y. Katayama. (2010) Density of dry peridotite magma at high pressure using an X-ray absorption method. *American Mineralogist*. **95**: 144-147.

Sakamaki, T., E. Ohtani, S. Urakawa, H. Terasaki, and Y. Katayama. (2011) Density of carboated peridotite magma at high pressure using an X-ray absorption method. *American Mineralogist*. **96**: 553-557.

Smyth, J. R. (1975) High temperature crystal-chemistry of fayalite. *American Mineralogist*, **60,** 1092-1097.

Sparks, R. S. J., R. A. Brooker, M. Field, J. Kavanagh, J. C. Schumacher, M. J. Walter, and J. White. (2009) The nature of erupting kimberlite melts. *Lithos*. **112S**: 429-438.

Spera, F. J. (1984) Carbon dioxide in petrogenesis III: role of volatiles in the ascent of alkaline magma with special reference to xenoliths-bearing mafic lavas. *Contributions to Mineralogy and Petrology*. **88**: 217-232.

Suzuki, A., E. Ohtani, and T. Kato. (1998) Density and thermal expansion of a peridotite melt at high pressure. *Physics of the Earth and Planetary Interiors*. **107**: 53-61.

Suzuki, A., and E. Ohtani. (2003) Density of peridotite melts at high pressure. *Physics and Chemsistry of Minerals*. **30**: 449-456.

Suzuki I. (1975) Thermal expansion of periclase and olivine, and their anharmonic properties. *J. Phys. Earth* **23,** 145-159.

Suzuki I., K. Seya, H. Takei, and Y. Sumino (1981) Thermal-expansion of fayalite, Fe_2SiO_3. *Physics and Chemistry of Minerals.* **7:** 60-6.

Taylor, S. R. (1992) *Solar System Evolution.* Cambridge University Press, New York, pp. 460.

Taylor, S. R. and McLennan, S. M. (2009) *Planetary Crusts.* Cambridge Planetary Science, New York, pp. 378.

Treiman A. H. (1995) Ca-rich carbonate melts: A regular-solution model, with applications to carbonatite magma + vapor equilibria and carbonate lavas on Venus. *American Mineralogist*. **80**: 115-130.

van Kan Parker, M., C. B. Agee, M. S. Duncan, and W. van Westrenen. (2011) Compressibility of molten Apollo 17 orange glass and implications for density crossovers in the lunar mantle. *Geochimica et Cosmochimica Acta*. **75**: 1161-1172.